Chemical Geology 650 (2024) 121994

Contents lists available at ScienceDirect

Chemical Geology

journal homepage: www.elsevier.com/locate/chemgeo

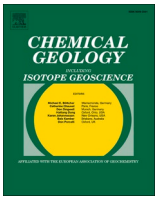

Coupled carbon-iron-phosphorus cycling in the Rainbow hydrothermal vent field

Kristin Anna Ungerhofer [a], Oliver Plümper [b], Martina Preiner [a,b,c,d], Gert-Jan Reichart [a,b], Peter Kraal [a,*]

[a] Royal Netherlands Institute for Sea Research (NIOZ), Department of Ocean Systems, Landsdiep 4, SZ 't Horntje 1797, the Netherlands
[b] Utrecht University, Faculty of Geosciences, Department of Earth Sciences, Princetonlaan 8a, Utrecht 3584 CB, the Netherlands
[c] Microcosm Earth Center, Hans-Meerwein-Str. 4, Marburg 35032, Germany
[d] Max Planck Institute for Terrestrial Microbiology, Karl-von-Frisch-Straße 10, Marburg 35043, Germany

ARTICLE INFO

Editor: Michael E. Boettcher

Keywords:
Iron nanoparticle
Phosphorus
Carbon
Hydrothermal plume
Mid-Atlantic Ridge

ABSTRACT

Hydrothermal venting has been shown to play a role in the global biogeochemical cycles of three bio-essential elements: iron (Fe), carbon (C) and phosphorus (P). However, our insight into the coupled cycling of Fe and associated C and P in hydrothermal plumes as well as their long-term fate in the underlying sediments remains limited. We present a detailed study, tracing the biogeochemical pathways of hydrothermally sourced Fe and the associated C and P from a buoyant to a neutrally buoyant plume and to the underlying sediments. Combining chemical and micro(spectro)scopic methods, we characterize particulate and dissolved phases recovered from the water column and sediment at two sites: one located directly in the active Rainbow hydrothermal vent field at 36°N on the mid-Atlantic ridge (MAR) and one located 3 km NE of the active vents. Our results show that the precipitates in one of the largest hydrothermal plumes on the MAR consist of aggregates of Fe nanoparticles, comprising poorly-ordered Fe oxyhydroxides and polycrystalline Fe sulfides, coated with carbon that is likely of organic origin. The sediments underlying the hydrothermal plume show enrichments in organic C, Fe, P and vent-derived trace metals such as Cu that decrease with distance from active vents. The enrichment in organic C and persistence of apparently highly-reactive Fe phases after sediment burial may reflect enhanced preservation potential of both phases as a result of the formation of organic-mineral complexes. We further demonstrate that the scavenging of dissolved seawater phosphate (PO_4^{3-}) by Fe nanoparticles is constrained to early stages of particle formation and sorption reactions in the buoyant hydrothermal plume and that P burial close to the vent field is driven by the deposition of the Fe nanoparticles. In the sediment, P is then efficiently retained through sink-switching from Fe-bound to more stable, authigenic apatite phases. As such, the sediments underlying the Rainbow vent seem to faithfully record coupled emission, scavenging and burial of essential elements and therefore offer potential for reconstruction of past venting activity. The deposition and burial of partly reduced plume material (e.g., Fe sulfides) in an oxic deep-sea sediment results in sediment chemistry and diagenesis that is very specific to the hydrothermal environment, while the redox signature of the plume is gradually lost. Beyond its role as a potential source of bioavailable Fe, we highlight how hydrothermal venting represents an efficient sink for organic C and bioavailable P. The findings contribute to understanding the profound impact of geological episodes of increased hydrothermal activity on ocean biogeochemistry and the coupled ocean-climate system.

1. Introduction

Hydrothermal venting has been shown to play a role in the global biogeochemical cycles of three bio-essential elements: iron (Fe), carbon (C) and phosphorus (P). Along the mid-ocean ridges, hydrothermal plumes which form when hot, reducing fluids are vented from the fractured seafloor, represent an important source of dissolved Fe(II) to the ocean (e.g., German et al., 2015; Tagliabue et al., 2010). A fraction of this Fe(II) is oxidized, precipitating in the near-bottom hydrothermal plume that forms over vent sites, and is subsequently removed from the

* Corresponding author.
E-mail address: peter.kraal@nioz.nl (P. Kraal).

https://doi.org/10.1016/j.chemgeo.2024.121994
Received 4 February 2023; Received in revised form 15 February 2024; Accepted 16 February 2024
Available online 17 February 2024

water column as it settles to the seafloor. However, recent work has shown that organic carbon (C_{org}) can bind Fe(II) and thereby enhance its lifetime and extend the range of transport (Bennett et al., 2008; Fitzsimmons et al., 2017; Hawkes et al., 2013; Sander and Koschinsky, 2011; Toner et al., 2009). Organic compounds in hydrothermal plumes may be sourced from (i) abiotic synthesis through the reduction of CO_2 with H_2 supplied during the serpentinization of peridotite in ultramafic-hosted vent systems (Holm and Charlou, 2001; Konn et al., 2009; Shock and Schulte, 1998) and/or (ii) particulate and dissolved C_{org} produced by chemolithoautotrophic communities living in/on the active chimney and in the plume itself (McCollom, 2000; Roohi et al., 2022). Alternatively to the stabilization and transport of Fe(II) in association with organic compounds, it has been hypothesized that what is commonly termed dissolved Fe(II) may in fact be nanoparticulate pyrite (FeS_2) that is operationally (i.e. filtration over 0.2 μm) defined as dissolved, which escapes oxidation due to its kinetic stability (Findlay et al., 2019; Gartman et al., 2014; German et al., 2015; Yücel et al., 2011).

Iron oxyhydroxides in the hydrothermal plume, forming by oxidation and precipitation of dissolved Fe(II), are prone to interact with many dissolved seawater species, such as the essential nutrient phosphate (referred to here as PO_4^{3-}; occurring predominantly as HPO_4^{2-} in seawater at pH 8) (Berner, 1973; Fröhlich et al., 1982; German and Seyfried, 2014). Negative PO_4^{3-} anomalies in the water column close to hydrothermal vents have been connected to scavenging by newly precipitated Fe oxyhydroxides in hydrothermal plumes (Feely et al., 1990, 1991; Wheat et al., 1996). The estimates of P removal by hydrothermal Fe particles have varied significantly over the last few decades. As more hydrothermal systems have been discovered and the characterization of their vent fluid and plume chemistry has developed, they are considered a significant sink in the global oceanic P budget, equivalent to 10–40% of the riverine input of dissolved inorganic P (Feely et al., 1990; Wheat et al., 1996; Wheat et al., 2003).

While the formation of Fe precipitates and aggregates in hydrothermal plumes is intensely studied, we lack insight into their long-term fate. This is important because long-term processes help determine the efficiency of hydrothermal venting as source or sink of elements, and control how hydrothermal processes are reflected in the geological record. In hydrothermal sediments from ~19°S on the southern East Pacific Rise (EPR), (Poulton and Canfield, 2006) found that a significant fraction of P released to interstitial waters during the diagenesis of poorly-ordered Fe oxyhydroxides is retained within the sediment by incorporation into more stable Fe minerals, precipitation as authigenic apatite and re-adsorption to poorly-ordered Fe oxyhydroxides. The role of the associated C_{org} in the early diagenesis of hydrothermal sediment deposits has not yet been elucidated, but the burial of C_{org} in association with Fe minerals in marine sediments in general, has been shown to create a long-term sink for C_{org} (Faust et al., 2021; Hemingway et al., 2019; Lalonde et al., 2012).

Here, we study the fate of hydrothermally sourced Fe in the Rainbow hydrothermal vent field, at 26° N on the mid-Atlantic ridge (MAR) at 2300 m below sea surface (mbss), southwest of the Azores. The hydrothermal fluid at Rainbow is exceptionally rich in dissolved Fe and the resulting hydrothermal plume is one of the most significant in terms of particle and Fe output (Charlou et al., 2002). The bulk chemistry of the vent fluid and underlying sediment has been studied previously (Cave et al., 2002; Charlou et al., 2002; Haalboom et al., 2020; Khripounoff et al., 2001) (see Section 2.1). However, so far, we lack insight into the properties of the Fe precipitates that form in the Rainbow plume and the (long-term) fate of Fe (and associated P) in the underlying sediment. Combining bulk and nano-scale characterization of hydrothermal precipitates in the buoyant and neutrally buoyant plume with the chemical investigation of the sediments below, we cover the diagenetic pathway of Fe and the associated C and P from mineral transformation in the young, buoyant plume to early diagenesis following the burial of hydrothermal precipitates at the seafloor. This combined approach allows us to shed more light on the complex coupling of the C-Fe-P cycle that ultimately controls their bioavailability as well as their long-term sequestration in the global ocean.

2. Materials and methods

2.1. Study sites

The Rainbow hydrothermal plume is emitted from the black smoker vents of the Rainbow vent field, located on the MAR, south of the Azores (Fig. 1A). At least ten groups of these high-temperature vents are scattered over an area of 100 × 200 m at approximately 2300 mbss on the western flank of the non-volcanic Rainbow Ridge (at 36° N), between the South Azores Mid Atlantic Ridge (S-AMAR) and AMAR segments of the MAR. Their hot (~ 365 °C), reducing effluent is sourced from ultramafic rock and bears a contrasting chemical signature to its purely basalt-hosted counterparts on the MAR (e.g., TAG, Lucky Strike) (Charlou et al., 2002; Douville et al., 2002). Key properties of the vent fluids are their low pH (2.8), high H_2S, H_2, CH_4 and CO concentrations as well as their significant enrichment in dissolved trace metals and rare earth elements (REE) (Charlou et al., 2002; Douville et al., 2002). Particularly their dissolved Fe (24 mmol L^{-1}) and Mn (2.25 mmol L^{-1}) concentrations rank among the highest observed in hydrothermal vent fluids. Upon emission from the vents, the effluent rapidly mixes with the ambient seawater, creating a hydrothermal plume that rises up to 200 m above the vent field, its dispersal in NNE-NE direction controlled by the local bathymetry and current regimes (German et al., 1998; Khripounoff et al., 2001; Thurnherr and Richards, 2001). In the sediments below the plume, enrichments in Fe, Mn and other trace metals, P and REE, result from the particle fallout at distances of 2–25 km from the Rainbow vent field (Cave et al., 2002; Haalboom et al., 2020).

During a research cruise on board RV Pelagia in July 2018, we selected two sampling sites, guided primarily by the detailed description of the active vents' location in Dyment (2009) and several studies of plume dispersal (e.g., Cave et al., 2002; German et al., 1998; Haalboom et al., 2020). At both sites we conducted turbidity profiling with a CTD as well as surveying with a tethered HD video frame (see Supplementary Information). The 'vent site' (36° 13.80′ N, 33° 54.2′ E) was located in the active vent field, and the 'distal site' (36° 14.86′ N, 33° 52.68′ E) lay 100 m higher on the western flank of the non-volcanic Rainbow Ridge (or Rainbow massif), approximately 3 km northeast, following the main direction of the prevalent currents and thus the main trajectory of the hydrothermal plume (Fig. 1B). At both sites we recovered samples of the dissolved and particulate phases in the water column and sediment.

2.2. Water column sampling and analyses

Chemical and physical water column properties were measured using sensors for conductivity (mS cm^{-1}, Seabird SBE4), temperature (°C, Seabird SBE3), beam transmission (%, WetLabs CStar transmissometer), turbidity (NTU, WetLabs FLNTU turbidity/chlorophyll sensor) and dissolved oxygen (μmol kg^{-1}, Seabird SBE43), mounted on a CTD-rosette with 24 Niskin bottles for water sampling (12 L each). The down-cast turbidity profile was used to determine the position of the hydrothermal plume. Across the plume interval, discrete sea-water samples were taken up-cast, in addition to samples above and below the plume and the surface water. Immediately after deployment and recovery of the CTD, 60-mL samples from each Niskin bottle were taken with a thrice-rinsed plastic syringe and filtered over 0.8/0.2 μm Supor filters for on-board spectrophotometric analysis of dissolved ammonium (NH_4^+), nitrate (NO_3^-), nitrite (NO_2^-) and phosphate (PO_4^{3-}) with a QuAAtro Gas Segmented Continuous Flow Analyzer (Grasshoff et al., 1983; Helder and De Vries, 1979; Murphy and Riley, 1958). Phosphate was also measured in unfiltered, acidified aliquots of the CTD water samples. The detection limit of the on-board method for phosphate measurement was 0.01 μmol L^{-1}.

Subsequently, two 30-mL aliquots from each water sample were

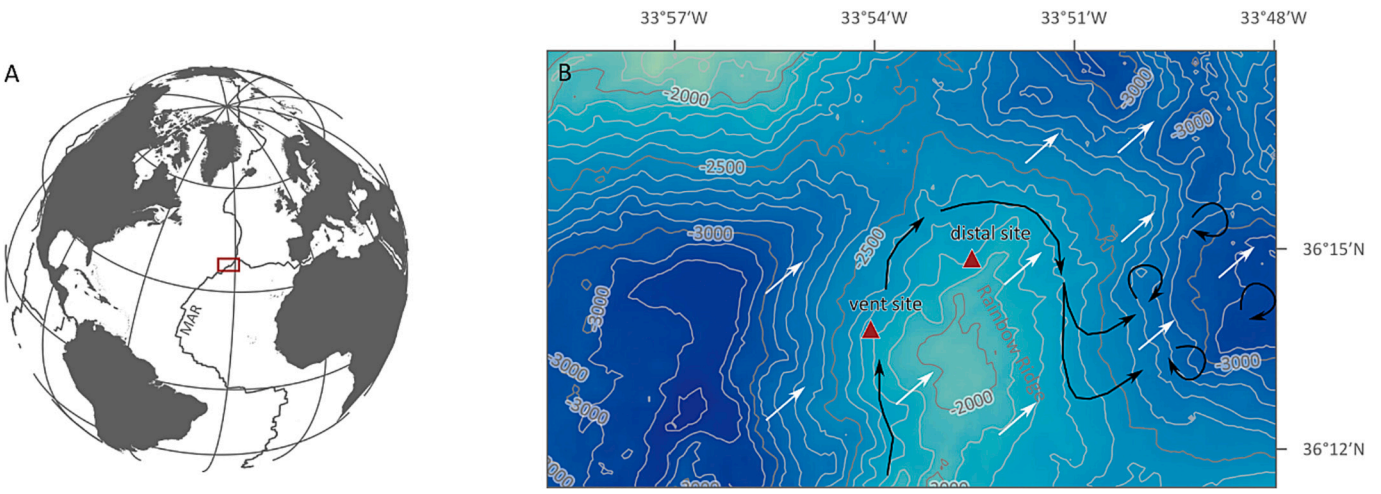

Fig. 1. (A) Location of the research area on the Mid-Atlantic Ridge. (B) Bathymetry of the Rainbow area (European Marine Observations and Data Network) with sampling sites. Arrows represent the mean flow regime around Rainbow Ridge (black below 2000 m, white above 2000 m) controlling hydrothermal plume dispersal, as described in Thurnherr and Richards (2001).

taken, one unfiltered and one filtered (0.2 μm Nylon syringe filter), to quantify total and dissolved element concentrations, from which particulate concentrations were estimated by difference. Here, we emphasize that the terms 'dissolved' and 'particulate' are used in the strictly operational sense of <0.2 μm and > 0.2 μm, respectively. The samples were acidified to pH ~ 1 with 450 μL 5 N ultrapure HCl and stored at 4 °C for (trace) element analysis at NIOZ. After dilution with an ultrapure HNO_3 standard, seawater concentrations of major and minor elements (Al, Fe, P, Mn, Cu) were determined in the filtered and unfiltered sample aliquots with a Thermo Scientific iCAP Q ICP-MS.

The remaining water from each Niskin bottle was filtered under nitrogen (N_2) overpressure using a gas-tight Advantec filter holder loaded with an acid-cleaned 0.2 μm polyethersulfone (PES) filter membrane (ø 47 mm) to collect suspended particulate matter (SPM). Air was removed from the filter units by allowing a small volume of water to run through before closing the filter holder gas-tight. The volumes of filtered water were recorded to enable the calculation of water column particulate concentrations on a volume basis. After a Niskin bottle was emptied, the filter units were kept connected for 10 min to remove as much water as possible from the filter under N_2 overpressure. After this, the filter units were taken off the bottles, closed off from the atmosphere, and immediately transferred into an N_2-purged glove bag to shield filtered material from oxidation by atmospheric oxygen. Inside the glove bag, the filters carrying suspended particulate matter (SPM) were removed from the filter holder using acid-cleaned plastic tweezers, placed into petri dishes, photographed and stored at −20 °C in N_2-purged, gas-tight sealed aluminum-laminate bags. In some cases, residual water in the filter unit caused a significant loss of particulate material during the removal of the filter from its holder (see Supplementary fig. 3). The filters were used for (i) total element analysis after acid digestion (Section 2.3) in the NIOZ trace metal laboratory, (ii) sequential Fe and P extraction (Section 2.4), and (iii) analysis of SPM by transmission electron microscopy (TEM) (Section 2.5).

2.3. Sediment sampling, pore water and solid-phase analysis

Following water column sampling, a video-guided box-corer was deployed to sample the surface sediment. Sub-cores were immediately taken in polycarbonate tubes (10 cm diameter) on deck. One core per site was sliced at a vertical resolution of 0.5 to 2 cm, with resolution decreasing with depth. The core from the vent site was very shallow: weathered bedrock was hit after about 8 cm of sediment and abundant rock fragments already occurred below ~3 cm depth. These fragments were removed and thus not included in the subsequent chemical analysis of the sediment. Per interval, approximately 10 mL of homogenized wet sediment were transferred into a pre-weighed plastic vial for on-shore porosity determination from gravimetric water loss (see Supplementary Information 1). The remaining sediment was transferred into a 50-mL polypropylene centrifuge tube that was thoroughly purged with N_2 and stored at −20 °C in N_2-purged gas-tight aluminum-laminate bags. Pore water samples were collected from a second core using rhizons with a 0.15 μm filter membrane (Rhizosphere Research Products B.V.) and sub-sampled for nutrient and trace metal analysis.

On shore, sediment samples were freeze-dried and ground with an agate mortar and pestle. Gravimetric water loss was used to determine porosity. Sub-samples of the dried and ground sediment and sections of the filters with SPM were used to determine concentrations of major and minor elements (Al, Fe, P, Mn, Cu) by Thermo Scientific iCAP Q ICP-MS after total acid digestion. For total acid digestion, about 100–125 mg of the freeze-dried and homogenized sediment and 1/8 or 1/16 of a PES filter with SPM were transferred into individual Teflon vessels and digested in a mixture of 2.5 mL HF, 1 mL HNO_3, 1.5 mL $HClO_4$, 1 mL HCl at 90 °C for 12 h. Subsequently, the acid mixture was evaporated to near dryness at 190 °C, after which the residue was re-dissolved in 20 mL (sediment samples) or 10 mL (SPM samples) of 1 M HNO_3 at 110 °C overnight.

For the sediment samples, the hydrothermal component $[E]_{\text{hydrothermal}}$ and enrichment factor (relative to the content in average deep-sea carbonate) EF_E of an element E (e.g., Fe, Cu, Mn, and P) were calculated using Eqs. (1–3):

$$[E]_{\text{background}} = (E/Al)_{\text{deep-sea carbonate}} * [Al]_{\text{sample}} \quad (1)$$

$$E_{\text{hydrothermal}}\ (\%) = \frac{\left([E]_{\text{total}} - [E]_{\text{background}}\right)}{[E]_{\text{sample}}} * 100 \quad (2)$$

$$EF_E = \frac{(E/Al)_{\text{sample}}}{(E/Al)_{\text{deep-sea carbonate}}} \quad (3)$$

Where $Al_{\text{deep-sea carbonate}}$ is the content of Al in deep-sea carbonate as reported in Turekian and Wedepohl (1961), and $(E/Al)_{\text{sample}}$ is the molar element/aluminum ratio in the sediment sample. Here we assume that the background sediment to which the hydrothermal component is added is carbonate ooze, which is the sediment type in this ocean region (Hayes et al., 2021). Contents in μmol g^{-1} were used in all calculations. In addition, the terrigenous index of Boström et al. (1973) was calculated as the Al/(Al + Fe + Mn) ratio (wt% $wt\%^{-1}$), reflecting the

contribution of hydrothermal metal-rich ('metalliferous') material. A value of 0.4 being the boundary between normal pelagic sediment (> 0.4) and metalliferous sediment with a high contribution of hydrothermal material (< 0.4).

Total carbon (TC) and total nitrogen (TN) contents in the sediment sub-samples were measured with a Thermo-Interscience Flash AE112 CN analyzer (Verardo et al., 1990). Total organic carbon (TOC) was measured in a separate sediment sub-sample from which carbonates were leached by placing it in a desiccator containing an open beaker of fuming HCl for 12 h and subsequently adding two aliquots of 30 μL 2 M HCl to each sample before re-drying them in the oven at 60 °C for one hour (modified protocol of Needoba et al. (2007).

To obtain information on bulk sediment mineralogy, subsamples of the freeze-dried and ground sediment from three selected depths (0.25, 1.75 and 6.5 cm) at the vent site were scanned from 0° to 80° 2θ using a 0.02° 2θ step and a 0.85 s count time on a Bruker-AXS D2 Phaser powder X-ray diffractometer equipped with Lynxeye detector and Cobalt Ka1,2 radiation source. Mineral identification by peak matching was performed in Bruker's DIFFRAC:EVA V6.0 using the Powder Diffraction File library.

2.4. Sequential extractions of iron and phosphorus from sediment and SPM

Chemical forms of Fe were characterized using the sequential extraction protocol of Kraal et al. (2017), based on Claff et al. (2010) and Poulton and Canfield (2005). Five pools of sedimentary iron were separated: (1) HCl-Fe(II) and HCl-Fe(III), (2) hydroxylamine-Fe, (3) dithionite-Fe, (4) oxalate-Fe, (5) HNO_3-Fe (Table 1). Tests with synthetic mineral standards have shown that 0.5 mol L^{-1} HCl quantitatively extracts highly disordered Fe(III) oxyhydroxides such as ferrihydrite, while dissolving only a minor proportion (< 10%) of poorly crystalline lepidocrocite (Kraal et al., 2022). Iron in all extracts was measured on a UV-VIS spectrophotometer with the Fe^{2+}-selective phenanthroline method (APHA, 2005). In the HCl extracts (step 1), Fe^{2+} and total Fe were determined by measuring absorbance before and after adding the hydroxylamine hydrochloride reducing agent that reduces dissolved Fe^{3+} to Fe^{2+}. The original Fe^{3+} concentration was calculated as the difference between total Fe and Fe^{2+}. The sum of these five Fe pools is commonly referred to as highly reactive Fe (FeHR) (Poulton and Canfield, 2005). Sedimentary P was separated into five pools using the SEDEX protocol (Ruttenberg, 1992) as adapted by Slomp et al. (1996): (1) Loosely-bound and exchangeable P, (2) CDB-P, (3) authigenic apatite, biogenic apatite and $CaCO_3$-associated P, (4) detrital apatite and other recalcitrant inorganic P phases, (5) organic P (Table 1). Phosphorus in the extracts of steps 1, 3, 4 and 5 was determined as the phosphomolybdate-blue complex by spectrophotometry (Murphy and Riley, 1958). Extracts of step 2, CDB-P, were measured using the adapted spectrophotometric procedure by Anschutz et al. (2005).

Table 1
Sequential extraction of phosphorus (P) and iron (Fe) chemical fractions.

Step	Target phase	Term	Extractant | extraction time | storage temp.
	Fe extraction method Step 1: modified Claff et al., 2010 |Step 2–5: Poulton and Canfield, 2005		
1	Highly-disordered or nanocrystalline ferrous and ferric Fe phases	HCl-Fe(II), HCl-Fe(III)	0.5 mol L^{-1} HCl (pH 0) | 1 h | 4 °C
2	Easily reducible Fe (oxyhdyr)oxides, e.g. lepidocrocite	Hydroxylamine-Fe	1 mol L^{-1} hydroxylamine - HCl solution 25% *v*/v acetic acid | 24 h | 4 °C
3	Crystalline Fe (oxyhydr) oxides, e.g. goethite, hematite	Dithionite-Fe	0.35 mol L^{-1} acetic acid / 0.2 mol L^{-1} Na_3 citrate / 50 g L^{-1} Na dithionite (pH 4.8) | 2 h | -20 °C
4	Recalcitrant Fe oxides, e.g. magnetite	Oxalate-Fe	0.17 mol L^{-1} NH_4 oxalate / 0.2 mol L^{-1} oxalic acid (pH 3.2) | 6 h | 4 °C
5	Pyrite	HNO_3-Fe	65% HNO_3 | 2 h | 4 °C
	P extraction method (SEDEX) Ruttenberg, 1992, Slomp et al., 1996		
1	Loosely-bound and exchangeable P	Exchangeable P	1 mol L^{-1} $MgCl_2$ (pH 8) | 30 min | 4 °C
2	Iron-associated P	CDB-P	0.3 mol L^{-1} Na_3 citrate / 1 mol L^{-1} $NaHCO_3$ / 0.14 mol L^{-1} Na-dithionite | 8 h | -20 °C 1 mol L^{-1} $MgCl_2$ (pH 8) | 30 min | 4 °C
3	Authigenic apatite, biogenic apatite and $CaCO_3$-associated P	Ca-P	1 mol L^{-1} Na-acetate (pH 4, acetic acid buffered) | 6 h | 4 °C 1 mol L^{-1} $MgCl_2$ (pH 8) | 30 min | 4 °C
4	Detrital apatite and other inorganic P phases	Detrital P	1 mol L^{-1} HCl | 24 h | 4 °C
5	Organic P	Organic P	Ashing at 550 °C | 2 h 1 mol L^{-1} HCl | 24 h | 4 °C

2.5. Analysis of plume particles using transmission electron microscopy (TEM)

Suspended particles collected on 0.2 μm PES filters from the plume interval at 2215 and 2265 mbss and from below the plume at 2316 mbss at the vent site were analyzed using TEM to determine their chemical composition, size and morphology. The particles were recovered from sections of the filter membranes through sonication in N_2-purged methanol-filled glass vials and drop-cast onto holey carbon on 200 mesh copper grids (Agar Scientific) inside an N_2-filled glove bag. In order to exclude organic contamination from the PES filters during the particle recovery process, we performed control analyses with synthetic Fe oxide nanoparticles (Fe(*II*,*III*)oxides, 100–200 nm, Sigma Aldrich). A 400 mL dispersion of 100 mg nanoparticles (3.5 *w*/*v*% NaCl, pH 8.5) was filtered through acid-cleaned 0.2 μm PES filters. The filtered nanoparticles were then treated equivalently to the natural samples. The grids were transported in membrane boxes (Agar Scientific) packed in N_2-purged aluminum laminate bags to Utrecht University for analysis in a FEI Talos F200X transmission electron microscope (TEM) operated at 200 kV. Using the scanning mode of the TEM (STEM), bright-field (BF), dark-field (DF), and high-angle annular dark field (HAADF) images were collected simultaneously from several areas on particles from each sampling depth. High-resolution (HR) imaging was done in TEM mode. High-sensitivity chemical mapping of several aggregates per water depth was performed by energy-dispersive X-ray (EDX) spectroscopy using the FEI Super-EDX setup. To mitigate the risk of beam damage, the microscope was aligned away from areas of interest, and nanoparticle aggregates were exposed to the electron beam for only a very brief period (a few seconds). Initially, low-dose TEM images were captured for an overview, followed by the collection of STEM images and X-ray maps. The beam was rastered across the sample over several minutes to prevent dose accumulation at any single point. Additionally, a comparative analysis of EDX map images, taken before and after the examination, revealed no significant changes in morphology, indicating that the structural integrity of the samples was largely preserved during analysis. Furthermore, diffraction patterns of Fe nanoparticles, recorded before and after the chemical analysis, showed no visible changes, suggesting minimal or no alterations in their crystal structure. This careful approach ensured the integrity of our results and minimized alterations to the samples during analysis. The analysis of all samples was performed using the Bruker ESPRIT software package, which facilitated comprehensive processing, peak deconvolution, and quantification using the Cliff-Lorimer method. A thickness of 100 nm and a density of 4.84 g/cm^3 for pyrite were assumed for the samples. This software enabled the clear identification of all peaks in the samples, including those of phosphorus, as demonstrated in Supplementary Fig. 6. To ensure accuracy, the background Cu and C signal were also

evaluated on an empty copper grid with holey carbon film. Our results indicate that the EDX intensity of the background Cu-Kα and C-Kα peaks (Supplementary fig. 7) only have minor contributions to the quantification of the nanoparticles composition and are within a 10% error range.

3. Results

3.1. Water column characteristics at the vent site: dissolved and particulate phases

At the vent site, deep waters between ~2200 and 2300 mbss showed elevated and highly variable turbidity up to 2.46 NTU, which is ~25 times higher than values in waters <2200 mbss (0.10 NTU) (Fig. 2A). This interval is referred to here as the 'hydrothermal plume interval' and is further characterized by raised temperatures (up to 4.3 °C compared to the ambient 3.8 °C, see Supplementary fig. 1), a non-linear relationship of conservative temperature Θ and absolute salinity S_A (see Supplementary fig. 2), and elevated concentrations of key elements such as Fe, Cu and Mn (Fig. 2A). The mean total Fe concentration in the plume interval measured in unfiltered, acidified seawater was 8 ± 4 μmol L^{-1} ($n = 8$), with a peak of 15 μmol L^{-1} at 2215 mbss. Iron was present in the plume predominantly (60–80%) in particulate form (> 0.2 μm), determined as the difference in Fe concentration between unfiltered and filtered seawater samples (Fig. 2A). Since the on-deck sampling of unfiltered and filtered seawater introduced a significant contamination risk for trace elements, caution is required when interpreting these absolute element concentrations. Therefore, we discuss the results regarding element enrichment or depletion in the plume relative to the control samples outside of the plume, indicated by the dotted lines in Fig. 2A and Fig. 6A. The SPM was collected in a closed system and therefore the risk of sample contamination was significantly reduced compared to the on-deck seawater sampling (see Section 2.2). The filter-SPM data, therefore, provide a means of quality control for the trace element measurements of the seawater samples. Particulate Fe concentrations determined from filtered and unfiltered seawater samples and SPM collection were similar, except for samples at 2205 and 2245 mbss, where material was lost during filter processing on board. The total Mn profile followed the same trend as Fe but with lower concentrations (mean 0.7 ± 0.4 μmol L^{-1}, n = 8). In contrast to Fe, filtered and unfiltered seawater samples showed that Mn was predominantly present in dissolved form, with <5% of Mn recovered in the >0.2 μm size fraction. Copper was below detection in the filtered and unfiltered seawater samples. However, Cu concentrations could be quantified in the digests of the SPM that was concentrated on PES filters. The mean particulate Cu concentration was 0.08 ± 0.08 μmol L^{-1} with elevated values up to 0.2 μmol L^{-1} in the plume interval. Total PO_4^{3-} concentrations measured in unfiltered, acidified CTD samples were stable at approximately 1.2 ± 0.01 μmol L^{-1} in the plume interval between 2200 and 2300 mbss, compared to 0.02 μmol L^{-1} in the surface waters. By contrast, dissolved PO_4^{3-} measured in filtered samples decreased from 1.1 to 0.2 μmol L^{-1} in the plume interval and showed a strong anti-correlation with total Fe (Pearson's $R^2 = -0.96$). The molar dissolved N:P ratios ranged between 14 and 17, close to the Redfieldian value of 16 typically found in marine algal biomass (Redfield, 1958) in surface water above the plume but reached values up to 108 in the plume interval.

Chemical sequential extraction applied to SPM on filter membranes showed that highly reactive Fe (Fe_{HR}) accounted for 60 ± 30% of total Fe as determined by total digestion (Fig. 2A). The relatively labile HCl-Fe(II), HCl-Fe(III), and hydroxylamine-Fe were the main Fe pools, together accounting for 94 ± 5% of Fe_{HR}. HCl-Fe(II) accounted for 12 ± 3% of Fe_{HR} and showed a strong positive correlation with HCl-Fe(III) (Pearson's $R^2 = 0.99$), the latter representing the biggest SPM Fe pool (80 ± 7% of Fe_{HR}). Phosphorus was detected only in the extracts of step 1 (exchangeable P) and 2 (CDB-P) of the chemical sequential extraction protocol (Fig. 2A). Due to the low concentrations of particulate P (0.3 ± 0.3 μmol L^{-1}), the measurement of P in the sequential extracts, even at minimal dilution, yielded values around the detection limit. Therefore, the P sequential extraction results do not provide reliable absolute concentrations of P fractions, but illustrate the presence of particulate P as exchangeable P and CDB-P.

3.2. Micro(spectro)scopic analysis of plume particles at the vent site

The (HR-)TEM images of suspended material collected from the plume interval (2215, 2265 mbss) and from below the plume (2316 mbss) at the vent site showed nanoparticles (several nm in diameter; Fig. 3B, C, D) occurring in aggregates (~ 300–900 μm in diameter; Fig. 3A, 4A). TEM-EDX analysis of 19 selected areas of interest on six different particle aggregates (Fig. 4C, Table 2, and Supplementary fig. 5) showed that the SPM consisted of Fe aggregates rich in C and Cu, with minor amounts of P, Zn, Si, and Al. While C, O, Fe, and P were more or less homogeneously distributed, Cu, Zn, and S showed localized enrichments. Selected area electron diffraction (SAED) patterns (Fig. 4B and Supplementary fig. 5) suggested that these Cu, Zn, and S enrichments are polycrystalline, in contrast to the more amorphous structure of the bulk material that mainly consisted of Fe and a matrix of C (Fig. 4C, Table 2 and Supplementary fig. 5). In Cu- and S-enriched areas, Cu:Fe and S:Fe ratios were up to 4 and 7 times higher compared to the amorphous Fe bulk material, respectively. The controls performed with filtered, synthetic iron oxide nanoparticles did not show any signals that would suggest that the C detected in the Fe-rich aggregates was an artefact from the used PES filters (see Supplementary fig. 5).

3.3. Bulk sediment chemistry at the vent site

Visual inspection of the sediment core from the vent site showed a thin, brown-red surface layer, about 3 cm thick (Supplementary fig. 4) with a low terrigenous index (0.02 ± 0.01, Fig. 2B) and low $CaCO_3$ content (4 ± 3 wt%, Fig. 2B), but with a strong hydrothermal signature (Table 3) and relatively high TOC content (1.2 ± 0.1 wt%, Fig. 2B). Iron and copper were strongly enriched in the surface layer, with peaks of 6000 μmol g^{-1} (33 wt%) and 2400 μmol g^{-1} (15 wt%), respectively (Fig. 2B). Concurrently, the highest solid-phase P contents of up to 170 μmol g^{-1} (0.53 wt%) were recorded in the top 3.5 cm of the sediment. Solid-phase Mn contents were markedly lower, showing a minor downcore increase from 40 to 11 μmol g^{-1}. Bottom water and porewater dissolved Fe^{2+} and Mn^{2+} concentrations were low and stable at 1 ± 0.1 and 1 ± 0.2 μmol L^{-1} in the top 3 cm. The pore-water PO_4^{3-}, NH_4^+ and NO_2^- concentrations were below 0.5, 0.8 and 0.3 μmol L^{-1}, respectively. Dissolved NO_3^- slightly increased from 18 to 20 μmol L^{-1} between bottom water and pore water of the top 1 cm and remained stable below. Below the top 3 cm was a thin, yellow-red layer of about 5 cm thickness with sediment characterized by a higher terrigenous index (0.2 ± 0.1, Fig. 2B) and $CaCO_3$ content (61 ± 13 wt%, Fig. 2B), but with a weaker hydrothermal signature (Table 3) and lower TOC content (0.6 ± 0.2 wt %, Fig. 2B). Iron and copper contents were significantly lower compared to the surface layer, approximately 600 μmol g^{-1} (3 wt%) and 100 μmol g^{-1} (1 wt%), respectively. In this sediment interval, solid-phase P contents dropped to 30 μmol g^{-1}. Manganese showed a slight down-core increase below the peak at 3.25 cm, from 11 to 70 μmol g^{-1}. Porewater sampling (with rhizons) below 3 cm was impossible due to the abundant rock fragments in the core (which were removed prior to chemical sediment analysis).

Highly reactive Fe at the vent site accounted for 89 ± 13% of the total sedimentary Fe pool, with HCl-Fe(III) representing the biggest fraction (56 ± 13%, 2023 ± 1332 μmol g^{-1}) of Fe_{HR} (Fig. 5A) and the sum of HCl-Fe(II), HCl-Fe(III) and hydroxylamine-Fe constituting 85 ± 8% of Fe_{HR}. Dithionite-Fe followed the total Fe profile and decreased with sediment depth (from approximately 500 to 200 μmol g^{-1}), yet its relative contribution increased below 3.25 cm depth from 7 to 22% of Fe_{HR} at the expense of HCl-Fe(II), HCl-Fe(III) and hydroxylamine-Fe.

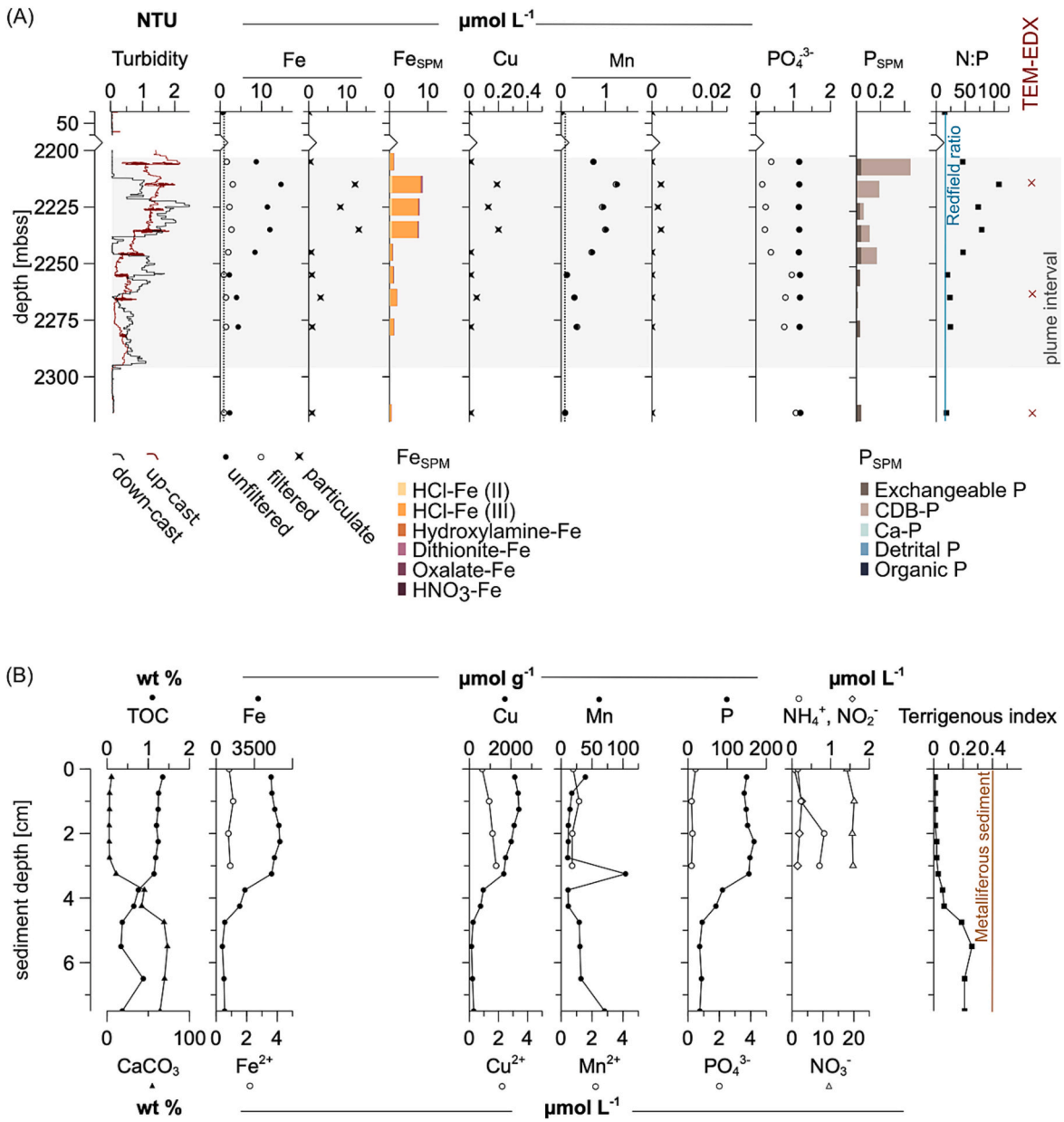

Fig. 2. Selected water column and sediment characteristics at the vent site. (A) Water column profiles of turbidity, Fe, Cu, Mn, and PO_4^{3-}, dissolved N:P and chemical fractions of Fe and P in the suspended particulate matter (SPM). Note the break of the vertical axes. The dotted lines in Fe and Mn profiles mark their concentrations measured in the surface waters. The shaded area marks the plume interval. (B) Sediment solid-phase (TOC, $CaCO_3$, Fe, Cu, Mn, and P) and pore water (Fe^{2+}, Cu^{2+}, Mn^{2+}, PO_4^{3-}, NH_4^+, NO_2^-, NO_3^-) profiles of key elements and solid-phase terrigenous index. Red crosses indicate depths from which SPM was analyzed with TEM-EDX. All data in this figure can be found in Supplementary Information 2. (For interpretation of the references to color in this figure legend, the reader is referred to the web version of this article.)

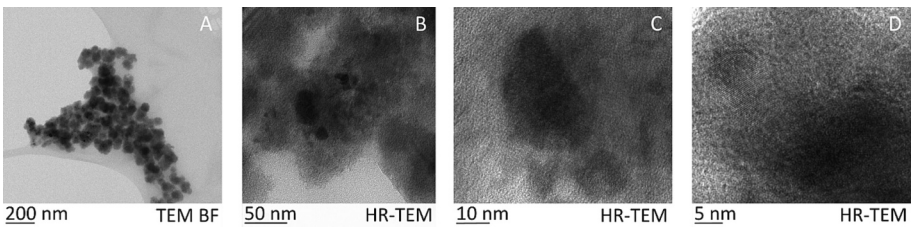

Fig. 3. HR-TEM images of aggregates of nanoparticles from 2265 mbss. Increasing magnification from A to D revealed (clusters of) nanoparticles of several nm in diameter occurring in aggregates of ~300–900 nm.

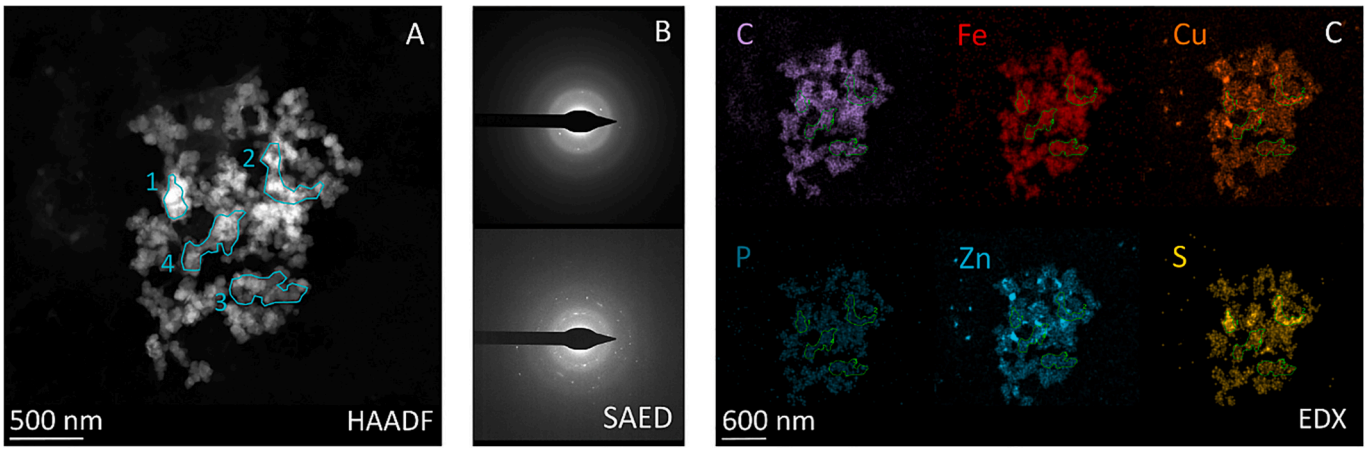

Fig. 4. (A) TEM HAADF image, (B) SAED patterns of amorphous/poorly ordered (upper) and polycrystalline (lower) areas and (C) quantified EDX element maps of a nanoparticle aggregate from 2265 mbss. The color scale was adjusted for each element to optimize the visibility of spatial distribution; color intensities cannot be compared between elements.

Table 2
Chemical composition of selected areas on the suspended particle aggregate from 2265 mbss shown in Fig. 4, based on TEM-EDX analysis. The complete dataset all 19 investigated areas (including errors) can be found in Supplementary Information 2.

Area	norm wt%									Element:Fe ratio			
	Fe	O	S	Cu	Zn	P	C	Si	Ca	Cu:Fe	P:Fe	S:Fe	C:Fe
1	26.1	27.1	5.7	5.9	1.2	0.9	31.0	0.5	1.8	0.2	0.03	0.2	1.2
2	27.1	27.9	5.1	5.7	1.3	0.8	30.2	0.6	1.3	0.2	0.03	0.2	1.1
3	23.5	33.1	1.3	2.6	1.2	1.0	35.2	0.7	1.5	0.1	0.04	0.1	1.5
4	24.8	31.6	2.2	3.6	1.6	1.1	32.0	1.0	2.2	0.1	0.04	0.1	1.3

Table 3
Comparison of hydrothermal components of P and selected transition metals in two depth intervals of the vent site and off-vent site sediment deposits.

Element	Rainbow sediment deposits						Carbonaceous deep-sea sediment [μmol g^{-1}][a]
	Vent site [μmol g^{-1}]	Hydro-thermal [%]	Enrichment EF_E	Distal site [μmol g^{-1}]	Hydro-thermal [%]	Enrichment EF_E	
	0–3.5 cm			0–14 cm			
Al	85			167			741
Fe	5361	100	334	260	86	7	161
Cu	2068	100	43,196	9	99	75	0.5
Mn	30	88	14	19	79	5	18
P	154	99	139	26	90	11	11
	3.5–8 cm			**14–28 cm**			
Al	180			211			741
Fe	1273	96	33	146	68	3	161
Cu	307	100	2559	2	92	14	0.5
Mn	31	79	7	18	69	3	18
P	48	93	18	12	74	4	11

Contents of oxalate-Fe and HNO_3-Fe showed a down-core decline, from 80 to 15 μmol g^{-1} and 130 to 2 μmol g^{-1}, respectively. These two Fe pools combined made up <5% of total Fe. The SEDEX extraction protocol recovered approximately 95 ± 12%[1] of total P in vent site sediments Fig. 5B). Similar to P in the SPM, the sedimentary P pool at the vent site was dominated by CDB-P (80 ± 15% of extracted P), reflecting the trend of surface enrichment and strong downward decrease of total solid-phase P. Ca—P was strongly enriched in the layer between 1 and 3.5 cm sediment depth (approximately 30–40 μmol g^{-1} compared to <10 μmol g^{-1} above and below), above the transition from Fe-dominated to $CaCO_3$-dominated sediment that occurs between 5 and 3 cm sediment depth. Detrital P showed a similar albeit much less pronounced enrichment at the same depth as Ca—P. Low levels of organic P were recorded throughout the core, its contribution to the total P pool declining from 1 to 4% with depth. The ratio of $TOC/P_{reactive}$ remained stable downcore, far below the Redfield ratio of 106 (Redfield, 1958) at 5 ± 3, with one significant increase at 6.5 cm depth coinciding with a peak of TOC content (Fig. 2B). The TOC/TN ratio, decreasing from 9 ± 0.5 in the top 4.5 cm to 5 ± 0.6 below showed a similar peak at 6.5 cm depth (Fig. 5B). By contrast, TOC/P_{org} varies strongly downcore, between 86 and 310.

3.4. Water column characteristics at the distal site: dissolved and particulate phases

At the distal site, turbidity was slightly elevated in a homogeneous

[1] Not including 2 outliers at 1.75 and 5.5 cm depth, where recovery was 120 and 129% respectively.

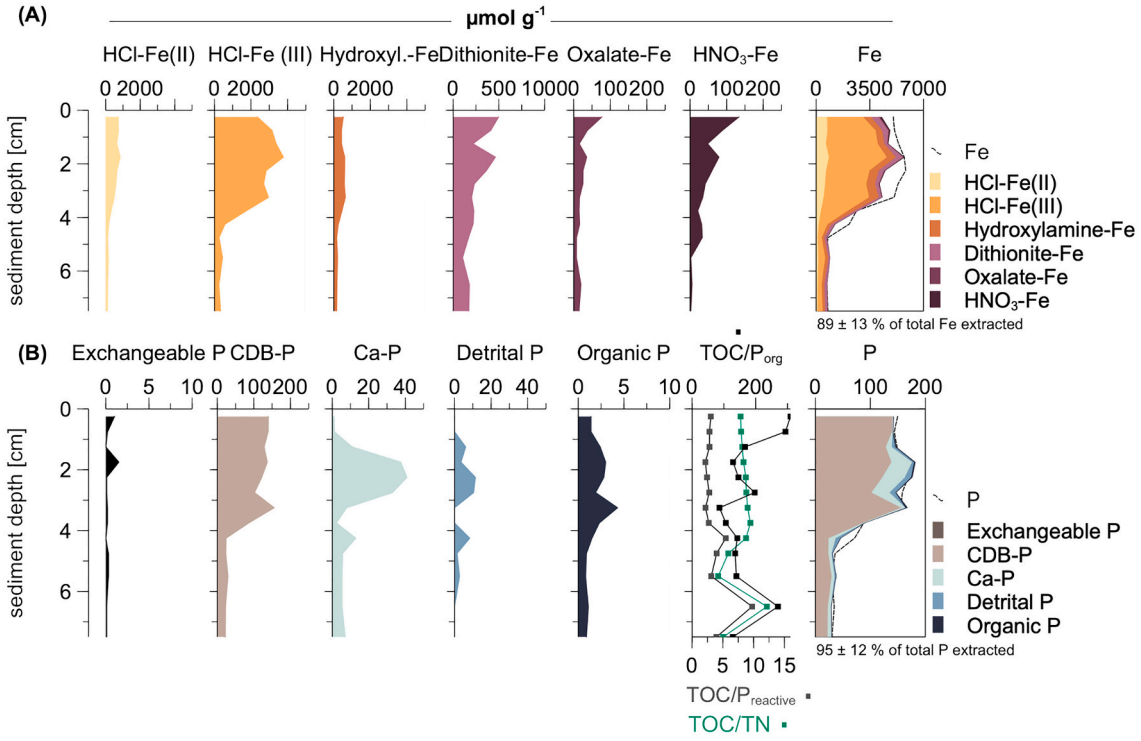

Fig. 5. Chemical fractions of (A) Fe and (B) P in vent site sediments, with cumulative contents of Fe and P depicted on the right. Ratios of TOC/P_{org}, $TOC/P_{reactive}$, and TOC/TN in vent site sediments. Detailed information on the chemical fractions is provided in Table 1. All data in this figure can be found in Supplementary Information 2.

and diluted plume interval between ~1900 and 2200 mbss, reaching values of 0.2 NTU (Fig. 6A). Copper, iron and manganese were enriched in the plume interval: Fe and Mn concentrations in the plume interval were on average 1 ± 0.2 μmol L^{-1} and 0.03 ± 0.01 μmol L^{-1}, respectively (Fig. 6A). The proportion of total Fe present in particulate form (> 0.2 μm) was 60–80% ($n = 8$), while the proportion of particulate Mn was >30% ($n = 5$). Copper was below the detection limit in the seawater samples and SPM analysis indicated relatively low Cu in the plume over the distal site (up to 2 nM, Fig. 6A). Total PO_4^{3-} concentrations (i.e. PO_4^{3-} measured in unfiltered, acidified water samples) were stable at 1.2 μmol L^{-1} in the deep waters, compared to 0.02 μmol L^{-1} in the surface sample from 3 mbss. Total and dissolved PO_4^{3-} concentrations were similar and the dissolved N:P ratio was stable at approximately 15 throughout the water column.

Chemical sequential extraction of SPM showed that highly reactive Fe (Fe_{HR}) accounted for 32 ± 22% of total Fe as determined by total digestion (Fig. 6A). The relatively labile HCl-Fe(II), HCl-Fe(III) and hydroxylamine-Fe represented the main pools, accounting for 71 ± 32% of Fe_{HR}. HCl-Fe(II) accounted for 26 ± 15% of Fe_{HR} and showed a positive correlation with HCl-Fe(III) (Pearson's $R^2 = 0.70$), the latter = representing the most important SPM Fe pool (44 ± 28% of Fe_{HR}). Phosphorus was measurable in the exchangeable P and CDB-P extracts. Due to the low concentrations of particulate P (0.01 ± 0.01 μmol L^{-1}), the measurement of P in the sequential extracts (also using minimal dilution) yielded values around the lowest calibration points. The P sequential extraction results therefore do not provide reliable absolute concentrations of P fractions, but suggest that particulate P was predominantly present as either exchangeable P or CDB-P.

3.5. Bulk sediment chemistry at the distal site

The surface sediment at the distal site was characterized by $CaCO_3$ contents ranging between 80 and 90 wt% (Fig. 6B). The terrigenous index was stable (0.4 ± 0.01) in the upper 12 cm of sediment, showing a slight downward increase to (0.6 ± 0.02) below this depth, concurrent with a down-core decrease in the hydrothermal component (Table 3). Organic carbon showed an opposite trend, declining from 0.4 wt% at the top to 0.1 wt% at depth (Fig. 6B). Solid-phase Fe and Cu contents in the calcareous sediment at the distal site were relatively high compared to 'normal' pelagic calcareous ooze. Iron and copper reached contents up to 270 μmol g^{-1} (1.5 wt%) and 9 μmol g^{-1} (0.1 wt%), respectively, in the upper part of the sediment core from the distal site, decreasing to 120 μmol g^{-1} (0.7 wt%) and 1 μmol g^{-1} (0.01 wt%) below 14 cm sediment depth. Manganese content was lower, 20 ± 3 μmol g^{-1}. Solid-phase P showed a similar pattern as Mn with highest values (up to 30 μmol g^{-1}) recorded in the top 14 cm, declining to 10 μmol g^{-1} below. Trends in bottom-water and pore-water trace metal and nutrient concentrations at the distal site were similar to those at the vent site. Dissolved Fe^{2+} was low and stable at 1 ± 0.1 μmol L^{-1} and Mn^{2+} was below detection throughout the core (Fig. 6B). Dissolved PO_4^{3-} increased from 1 to 4 μmol L^{-1} in the top 8 cm, with minimal variation below. Pore-water NH_4^+ and NO_2^- levels were below 4 and 0.2 μmol L^{-1} respectively,[2] and NO_3^- showed a downcore increase from 23 μmol L^{-}in the bottom water to 36 μmol L^{-1} in the deepest sample.

Highly reactive Fe made up 77 ± 11% of total Fe in the sediments of the distal site (Fig. 7A). Of total Fe, HCl-Fe(III) was the dominant Fe pool (37 ± 11% of Fe_{HR}, 70 ± 36 μmol g^{-1}) and the labile Fe phases represented by HCl-Fe(II), HCl-Fe(III) and hydroxylamine-Fe made up 70 ± 10% of Fe_{HR}. Both total contents of dithionite-Fe (44 ± 8 μmol g^{-1}) and its relative contribution to Fe_{HR} (27 ± 7%) remained relatively stable downcore. Oxalate-Fe was not present above 1.75 cm and showed a slight downcore increase to a peak of 15 μmol g^{-1} at 25 cm depth. The HNO_3-Fe contents remained <5 μmol g^{-1}. The SEDEX extraction protocol recovered approximately 76 ± 10% of total P in distal site sediments (Fig. 7B). The CDB-P represented the most important P pool at the

[2] Deepest sample is an outlier with NH_4^+ concentration of 3.3 μmol L^{-1}.

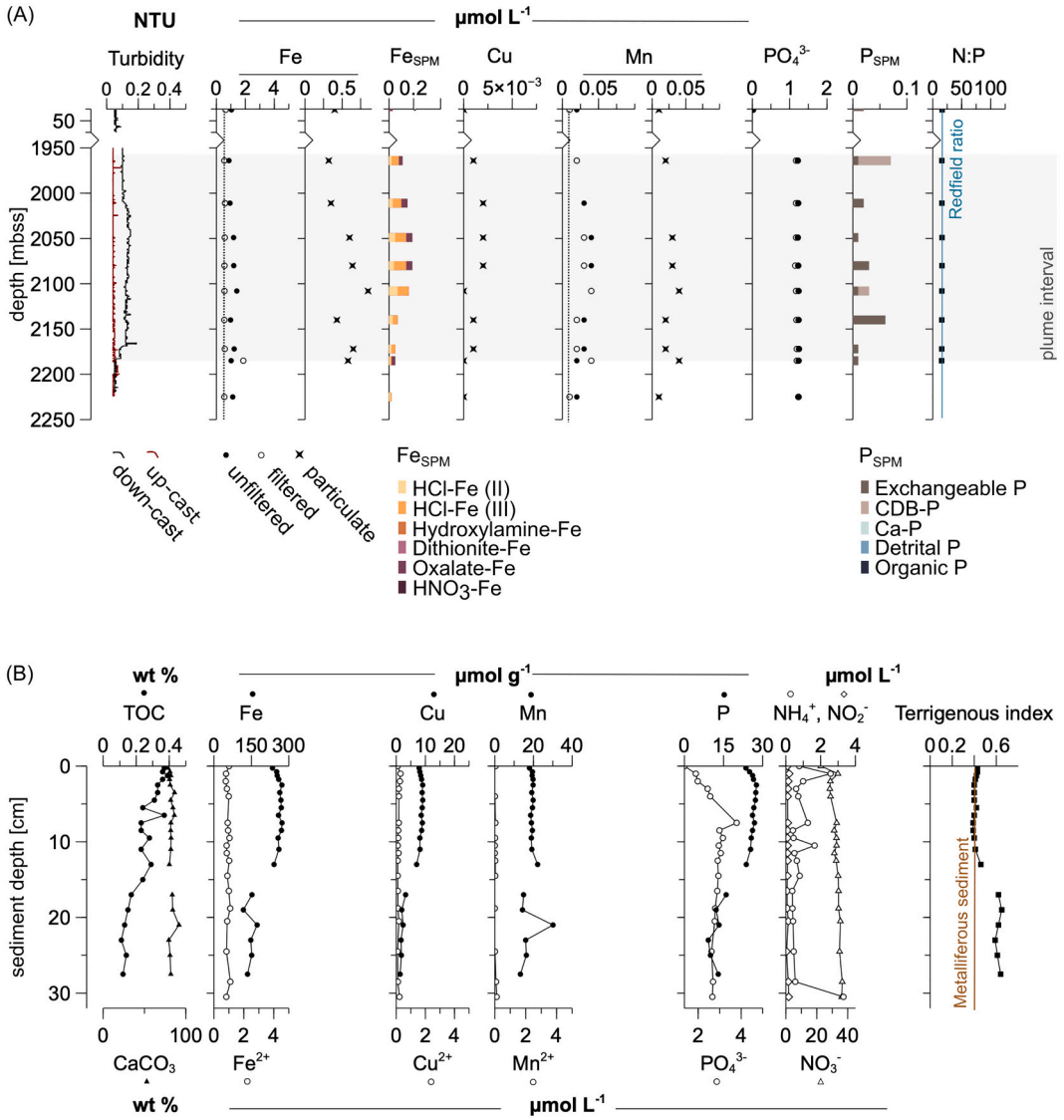

Fig. 6. Selected water column and sediment characteristics at the distal site: (A) Water column profiles of turbidity, Fe, Cu, Mn and PO_4^{3-}, dissolved N:P and chemical fractions of Fe and P in the suspended particulate matter (SPM). Note the break of the vertical axes and break of the Fe_{SPM} horizontal axis. The dotted lines in Fe and Mn profiles mark their concentrations measured in the surface waters. The shaded area marks the plume interval. (B) Sediment solid-phase (TOC, $CaCO_3$, Fe, Cu, Mn and P) and pore water (Fe^{2+}, Cu^{2+}, Mn^{2+}, PO_4^{3-}, NH_4^+, NO_2^-, NO_3^-) profiles of key elements and solid-phase terrigenous index. All data in this figure can be found in Supplementary Information 2.

distal site (53 ± 14% of total P), following the trend of enrichment in the top 14 cm and downward decrease as observed for total solid-phase P. Low levels of Ca—P, Det-P and organic P were recorded throughout the core, contributing 21 ± 8%, 7 ± 4% and 3 ± 1% to total P. The ratio of $TOC/P_{reactive}$ remained stable downcore, far below the Redfield value of 106 (Redfield, 1958) at 7 ± 2, with one significant increase at 0.75 cm depth coinciding with a peak in TOC content (Fig. 2B). The TOC/TN ratio varied around 4 ± 2 (Redfield = 6.6) and showed a slight downcore decrease. By contrast, TOC/P_{org} varied strongly downcore, between 104 and 278 (Fig. 7B).

4. Discussion

4.1. Composition and transport of hydrothermal plume particles

Above the vent site, video footage recorded before sampling (see Supplementary video) showed a highly dynamic hydrothermal plume rising rapidly through the water column, likely originating from several of the closely spaced black smokers in the Rainbow vent field (German et al., 1996). The elevated and highly variable turbidity as well as the high Fe and Mn concentrations (Fig. 2A) indicate that a young stage of the Rainbow hydrothermal plume was intercepted at the vent site. The non-linearity in the relationship of conservative temperature Θ and absolute salinity S_A (see Supplementary fig. 2), and plume interval temperatures close to the ambient sea water temperature, further suggest that the young, buoyant but already well-mixed plume was sampled. Bulk chemical and TEM-EDX analysis of the SPM provide detailed insight into the composition of the particles in the hydrothermal plume at this stage. Our Fe extractions capture a range of highly disordered to poorly crystalline Fe(III) and Fe(II) phases. Hydrochloric acid-extractable Fe(II) indicates the presence of metastable Fe monosulfide or nanoparticulate pyrite, while HCl-Fe(III) and hydroxylamine-Fe indicate poorly-ordered Fe (oxyhydr)oxides (Fig. 2A, 6A) in the SPM. Correspondingly, high-resolution TEM reveals that the SPM is in fact comprised of aggregates of nanoparticles (Fig. 3). Quantification of EDX data shows that the bulk of these aggregates consists of C, O, Fe and P, with local (spatially overlapping) enrichments of Cu, S and Zn (Fig. 4C, Table 2). Furthermore, selected area diffraction (SAED) analysis

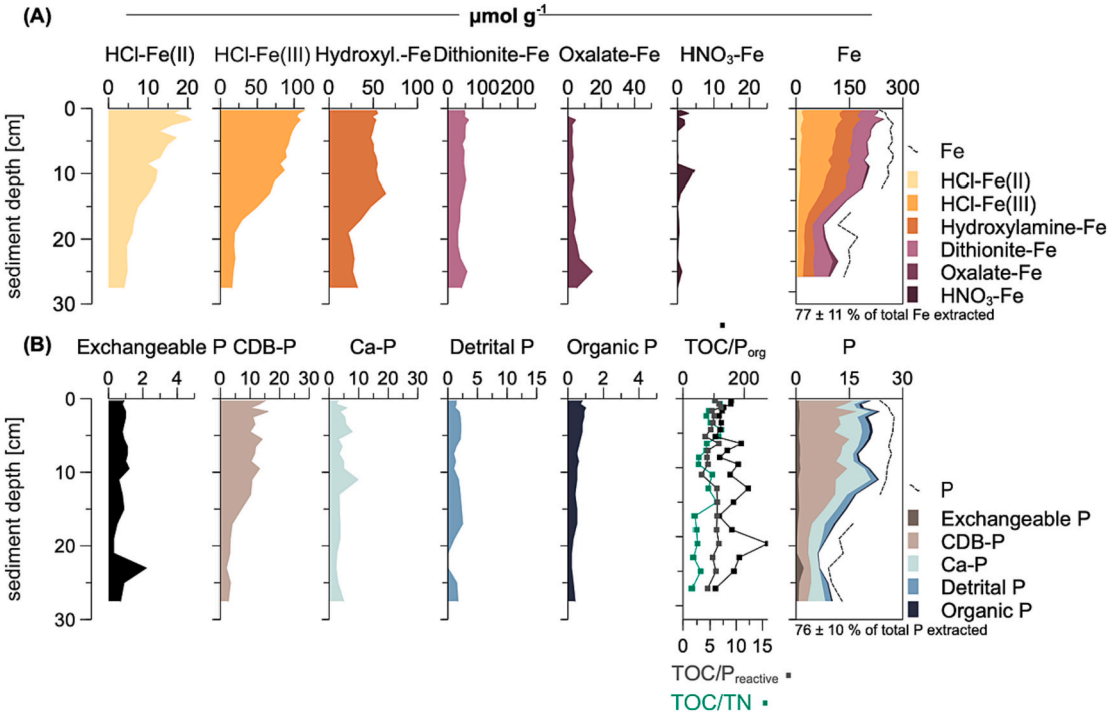

Fig. 7. Chemical fractions of (A) Fe and (B) P in distal site sediments, with their cumulative contents of Fe and P depicted on the right. Ratios of TOC/P_{org}, $TOC/P_{reactive}$, and TOC/TN in distal site sediments. Detailed information on the chemical fractions is provided in Table 1. All data in this figure can be found in Supplementary Information 2.

(Fig. 4B) shows the bulk of the aggregates to be structurally amorphous compared to the polycrystalline areas of Cu, S, and Zn enrichment.

Our data does not provide direct evidence for the nature of C in these nanoparticle aggregates. However, the amorphous structure of the bulk of the aggregates and the high TOC content of the top sediment layer below the buoyant plume at the vent site (Fig. 5B) strongly suggest that C_{org} is an important component of the nanoparticle aggregates. Further support for the presence of C_{org} in the nanoparticle aggregates comes from recent work by Roohi et al. (2022), who demonstrated that the plume represents an important source of C_{org} to the near-field sediments at Rainbow. In general, C_{org} has been found to be pervasive in hydrothermal plumes (Bennett et al., 2008; Fitzsimmons et al., 2017; McCollom, 2000; Toner et al., 2009). In the young, buoyant Rainbow hydrothermal plume C_{org} may originate from two sources: (i) dissolved and particulate organic compounds produced by the chemolithoautotrophic communities thriving on/close to the vent and in the plume itself (Haalboom et al., 2020; Roohi et al., 2022) and (ii) abiotically synthesized organic compounds that have been shown to constitute a non-negligible component of vent fluids in ultramafic-hosted hydrothermal systems (Holm and Charlou, 2001; Konn et al., 2009).

Areas of polycrystalline Cu, S and Zn enrichment in the mineral-organic aggregates may represent dense chalcopyrite $FeCuS_2$ and possibly sphalerite (ZnFe)S, both of which form already inside the vent before the expulsion of the vent fluid (German and Seyfried, 2014). Polycrystalline nanoparticulate Fe sulfides have been recovered from nascent hydrothermal plumes of high-temperature vents at the EPR and Lau Basin (Findlay et al., 2019; Yücel et al., 2011) and Rainbow (Gartman et al., 2014) and are hypothesized to represent a kinetically stable form of Fe(II) that may be transported over longer distances in the hydrothermal plume. Complementary to their work, which was focused on samples recovered from a maximum distance of 1 m from the vent orifice (Findlay et al., 2019; Gartman et al., 2014; Yücel et al., 2011), we demonstrate that these nanoparticulate sulfide phases persist at least into the buoyant plume stage, several hundreds of meters away from the vent orifice, aggregated with poorly-ordered Fe oxyhydroxides. Iron sulfide phases likely do not play a significant role in P transport and transformation, because of their low relative abundance in the investigated SPM and sediment and their low affinity for P (Krom and Berner, 1980).

Marked shifts in molar element:Fe ratios were observed between the hydrothermal plume SPM and the surface sediment at the two investigated sites (Fig. 8). These shifts indicate the preferential settling of aggregates enriched in iron-sulfide phases near the vent field. The Cu:Fe ratios observed in the Rainbow near-field sediments are up to 24 times

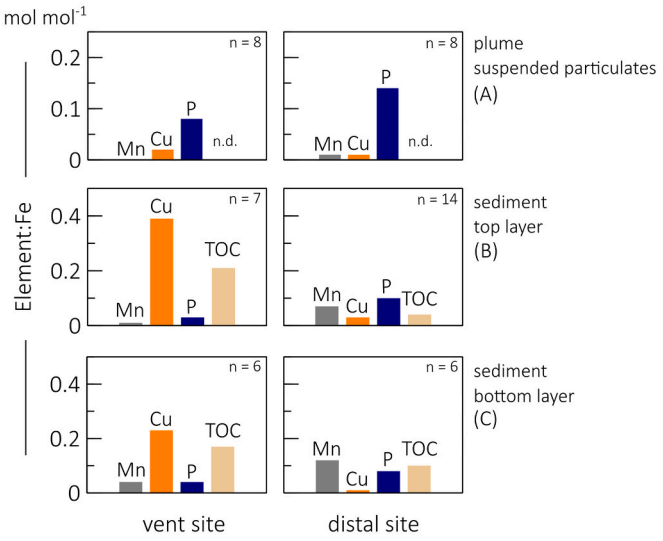

Fig. 8. Molar element:Fe ratios for P, Mn, Cu and TOC from the vent to the off-vent site in (A) the suspended particulates, (B) the Fe-rich top sediment layer, (C) the carbonaceous bottom sediment layer. C:Fe ratios of the suspended particulates from the plume interval at the vent site vary around 2 ± 0.8, based on TEM-EDX data.

higher than in the SPM and decrease with distance from the vent (Fig. 8). A dramatic decrease in sedimentary Cu contents by a factor of ~200 from the vent to the distal site (Fig. 2B, 6B) supports the conclusion drawn by (e.g., Cave et al., 2002; Edmonds and German, 2004; Haalboom et al., 2020; Trocine and Trefry, 1988) that Cu associated to sulfide-bearing Fe phases (e.g., chalcopyrite or sphalerite) is quickly removed from the plume. This is supported by the surface enrichment of HNO_3-Fe (Fig. 5A) captured by our sequential extraction and partly by our XRD data (Supplementary fig. 8), indicating the presence of the chalcopyrite, pyrite and potentially pyrrhotite ($Fe_{(1-x)}S$) at 0.25 and 1.75 cm depth in vent site sediments. However, the XRD analysis also revealed that not all Cu is necessarily associated with Fe particles, but also transported in the plume as copper halide (clino/para-)atacamite (CuZnClOH). Elevated Cu concentrations in the SPM and the sediments at the distal site (Fig. 6A, 7A) suggest that a fraction of the Cu detected in the buoyant plume is still present several kilometers from the Rainbow vent orifices. Nanoparticulate Cu phases may therefore bear the potential for longer-range transport within the hydrothermal plume, noting that the scale of our study with sites located only a few kilometers apart does not allow us to extend these findings to the ocean scale. The surface enrichment of HCl-Fe(II) further indicates the presence of metastable Fe monosulfide or nanoparticulate (chalco)pyrite in the distal site sediments, meaning that at least a part of nanoparticulate Fe(II) escapes oxidative precipitation in the plume in the form of chalcopyrite, aggregated with poorly-ordered Fe oxyhydroxides and (organic) carbon.

González-Santana et al. (2021) demonstrate that the presence of organic ligands in hydrothermal plumes may delay the oxidation of Fe (II), supporting our assumption that complexation to organic compounds may stabilize Fe(II) species in the aggregates and thereby extend their transport range. Complexation of organic carbon can affect the chemical properties of hydrothermal Fe particles, by preserving Fe(II) and inhibiting crystallization of Fe(III) precipitates. Furthermore, organic-rich Fe aggregates provide micro-environments in plume particles for biotic Fe(III) reduction (Li et al., 2014). We also note that the formation of organic-rich aggregates will decrease their density and settling speed compared to iron minerals (Cornell and Schwertmann, 2003; Bhattarai et al., 2018) and thereby potentially enhance the range of transport.

The SPM that remains suspended in the hydrothermal plume for at least several kilometers comprises aggregates that still contain a small amount of Fe sulfides, but are predominantly composed of P-rich Fe oxyhydroxides (Fig. 2A, 6A). An increase of the P:Fe ratios from the vent to the distal site in the plume as well as the surface sediment (Fig. 8) confirms that mainly aggregates of P-rich Fe oxyhydroxides are transported away from the vent field, while P-poor Fe sulfides are removed from the plume at an earlier stage. This contradicts results provided by Cave et al. (2002) and Edmonds and German (2004), who find P:Fe ratios to remain constant between particles of the buoyant, neutrally-buoyant plume and the surface sediment. This discrepancy in findings might be due to a difference in the filtration of seawater samples, capturing different Fe and P phases. While the samples discussed in Cave et al. (2002) and Edmonds and German (2004) were recovered with filters of 1 μm pore size, our samples were recovered with filters of 0.2 μm pore size. The detected change in bulk P:Fe ratios of SPM due to the preferential persistence of P-rich nanoparticle aggregates elucidates the key role of smallest (colloidal) particles in the impact of hydrothermal venting on ocean chemistry.

In contrast to Fe, 60–80% of which is present in particulate form (> 0.2 μm) in the buoyant plume at Rainbow, Mn concentrations in the SPM are low relative to Fe despite its 10^6-fold enrichment in the Rainbow vent fluids relative to seawater. This reflects the slow Mn(II) oxidation kinetics and precipitation compared to Fe (Tebo et al., 2004). Consequently, Fe precipitates and settles much more quickly from the plume than Mn (Cave et al., 2002; Haalboom et al., 2020). This leads to an increase of the molar Mn:Fe ratio in SPM by two orders of magnitude (Fig. 8) and an increase in the proportion of dissolved Mn (Fig. 2A, 6A) between the vent site and the distal site. Consequently, the amount of Mn deposited is several orders of magnitude smaller than the amount of Fe deposited in the vent and the distal site sediments (Fig. 2B, 6B), and sedimentary Mn contents are similar to those of an average carbonaceous deep-sea ooze (Table 3). This limited burial of hydrothermal Mn at both the vent and distal site reflects the potential for long-range transport of Mn (also a key element in biogeochemistry) from hydrothermal vents, again noting that conclusions about ocean-scale processes cannot be drawn from the current study.

4.2. Deposition and diagenesis of hydrothermal plume particles

The flux of particles from the hydrothermal plume to the surrounding seafloor is variable in time due to variations in venting intensity and changes in the flow pattern of the plume itself. On the western flank of Rainbow Ridge, where the vent site is located, Cave et al. (2002) reported accumulation rates of Fe, Cu, P and Mn in Holocene sediments to be 5 to 10 times higher than in older sediments. In this study, the bulk sediment chemical characteristics at both sites show that the signature of hydrothermally derived material is more pronounced in the top layer. At the vent site, as metal contents increase, we see a substantial shift in the terrigenous index at 3.5 cm sediment depth (Fig. 2B). At this location in the active vent field, a reliable reconstruction of sediment age was not possible. We suppose that the sudden transition to sediment with a strong hydrothermal signature may reflect the establishment of a new black smoker in the immediate vicinity. Average sedimentation rates do not apply here, as particle fluxes are much higher and much more variable than at 3-km distance from the vent field (Khripounoff et al., 2001). The hydrothermal layer of the vent site sediments therefore does not provide information about the overall intensity of venting. At the distal site, the upward increase in hydrothermal component (by 10–20%; Table 3) and decrease in terrigenous index (from 0.4 to 0.6; Fig. 6B) between 17 and 11 cm sediment depth suggest that the younger sediment records more intense hydrothermal venting and is therefore enriched in TOC, Fe, P and Cu (Fig. 6). Based on a recent estimate of the average sedimentation rate in this area (approx. 3 cm kyr^{-1} by (Van Loon, 2016)) the distal site sediment record may cover ~11 kyrs of deposition of hydrothermal plume fallout. The transition commences at ~17 cm, corresponding to an estimated onset of intensified venting approximately 6 kyrs ago, not considering any uncertainties due to bioturbation. This is in agreement with the results presented by Cave et al. (2002), who determined that the transition may be timed between 8 and 12 ^{14}C kyr BP.

Our chemical Fe fractionation data show a reverse diagenetic signal of pyrite-Fe (HNO3-Fe) (Fig. 5A, 7A), decreasing with depth as it seemingly undergoes oxidation after accumulating as a result of the rapid fallout of nanoparticulate chalcopyrite and other Fe-sulfides from the buoyant hydrothermal plume. This means that while the sediments may record the intensity of the hydrothermal venting, the oxidation state and speciation of the Fe-minerals are not preserved long-term. The persistence of sedimentary HCl-extractable Fe at both sites (Fig. 5A, 7A) may indicate that the progressive transformation of poorly-ordered Fe oxyhydroxides (e.g., ferrihydrite) to more stable phases (to e.g., hematite, goethite, magnetite) during burial is inhibited. While experimental evidence suggests that poorly-ordered ferrihydrite may be transformed to the thermodynamically more stable minerals hematite and goethite within years at the pH of seawater ~8 and bottom water temperatures around 4 °C (Cornell and Schwertmann, 2003; Poulton and Canfield, 2006), we find that a significant proportion of HCl-Fe(III) and hydroxylamine-Fe (assumed to represent highly reactive, poorly-ordered Fe (oxyhydr)oxides) is preserved for several thousands of years at the distal site (Fig. 7A). This is indicative of a diagenetic setting similar to that of the southern EPR sediments studied by Poulton and Canfield (2006), who reported a slow rate of ferrihydrite transformation and the long-term stabilization of a proportion of hydrothermal ferrihydrite. Several factors may play a role in inhibiting the diagenetic

transformation of poorly ordered Fe minerals to more stable phases, among others the sorption of oxyanions (such as PO_4^{3-}) and transition metals (Cornell and Schwertmann, 2003; Zhao et al., 1994).

However, it is also possible that the HCl step extracted Fe precipitates that had crystallized but remained nanocrystalline and were therefore highly soluble (Van der Zee et al., 2003) Fe minerals. The persistence and/or nanocrystalline nature of the hydrothermally sourced Fe minerals in the sediments means that they retain their high sorption capacity (for PO_4^{3-} and dissolved organic compounds, for example) and that the diagenetic alteration of the sediment composition remains limited. The persistence of reactive, either poorly-ordered or nanocrystalline, Fe (oxyhydr)oxides over such timescales suggests that nano-scale aggregates may play a role in long-range transport of hydrothermal Fe in the ocean. Considering that the SPM of the hydrothermal plume is composed of carbon-coated nanoparticulate iron aggregates and we see a down-core correlation of C_{org} and highly reactive Fe-minerals at both investigated sites (Fig. 2B, 5A, 6B, 7A), we propose that the aggregation of Fe-minerals with C_{org} is a major controlling factor of mineral preservation, not only during suspension in the plume, but also in the context of long-term burial. Conversely, highly reactive Fe minerals have been discovered to play a crucial role in preserving C_{org} over millennial time scales in different marine environments by shielding it from remineralization (Faust et al., 2021; Hemingway et al., 2019; Lalonde et al., 2012). This preservation mechanism may turn hydrothermal vent fields into efficient 'rusty sinks' for organic matter, particularly near active vents, where TOC contents (1.2 ± 0.1 wt% in top layer) are relatively high compared to average deep-sea sediments (0.3 wt%according to (McIver, 1975)) (Fig. 2B). More importantly, the relatively high sedimentation rates result in enhanced C_{org} burial rates. Associations in the early plume stages, therefore, affect Fe and P burial (and global cycling) as well as C burial.

4.3. Phosphorus sorption, burial and diagenesis

The Fe(III) (oxyhydr)oxides precipitating in the hydrothermal plume can readily take up dissolved PO_4^{3-} during and after their formation (e.g., Berner, 1973; Feely et al., 1990; Wheat et al., 1996). This removal is discernable as a marked decrease in dissolved PO_4^{3-} concentrations from approximately 1 mol L^{-1} to as little as 0.2 mol L^{-1} (average NADW concentration 1.1 ± 0.05 μmol L^{-1}) that correlates with a peak in total Fe concentrations in the plume interval at the vent site (Fig. 2A), while total PO_4^{3-} shows a straight water column profile. The correlation of the HCl-extractable fractions of both Fe and P in the suspended particles confirms that Fe oxyhydroxides are responsible for P removal. The lack of PO_4^{3-} depletion at the distal site (Fig. 6A) indicates that the Fe precipitates are saturated with P early on in their formation, fitting with sorption during and shortly after Fe(III) precipitation. Coprecipitation with PO_4^{3-} would also enhance the disorder of the Fe(III) minerals (Kraal et al., 2019, 2022; Voegelin et al., 2013), potentially slowing their transformation within the plume.

The fallout of P-rich Fe oxyhydroxides results in a strong sedimentary P enrichment at the vent site and P contents up to twice as high as in average deep-sea calcareous oozes (Table 3) at the distal site. Accordingly, Fe-bound P (CDB-P, Fig. 5B, 7B) represents the most important P pool at both sites. The close relationship between transport and deposition of Fe and P and venting intensity is further highlighted by the concomitant increase of both total P and Fe-bound P with a drop in the hydrothermal index in the top layers of the sediment at both investigated sites (Fig. 2A, 6A), suggesting that the venting intensity controls P burial. Organic P, assumed to be the main carrier phase of P in an oceanic setting (Ruttenberg, 2014), is a minor P sink (< 5% of total P) at both sites (Fig. 5B, 7B). This could be because of rapid organic P mineralization in the sediment. However, assuming efficient retention of remineralized P in the sediment, the ratio of TOC to total reactive P should then be close to the C/P ratio of the original organic P source. The C/P ratio in organic matter is likely close to 106, the Redfield ratio for marine algal material (Redfield, 1958). However, we measure very low sedimentary TOC:Preactive ratios of 5 ± 3 at the vent site and 7 ± 2 at the distal site. This indicates that additional P is supplied to the sediment, likely in the form of Fe-associated P that was scavenged from the water column by plume particles. The high and variable sedimentary TOC:P_{org} ratios at the vent site (86–310) and the distal site (104–278; Fig. 7B) may result from diagenetic increase of TOC/Porg above 106 by preferential loss of P-rich compounds (Anderson et al., 2001). Furthermore, there may be a contribution of microbial biomass; chemolithoauto and -heterotrophic bacteria occur in the Rainbow plume (Haalboom et al., 2020) and the C/P ratio of marine bacteria can vary strongly depending on conditions with values far exceeding the Redfield ratio of 106 (Fagerbakke et al., 1996; Vrede et al., 2002).

The aggregates of highly reactive Fe oxyhydroxides to which the main P pool is associated undergo a slow transformation to more stable mineral phases during burial. A fraction of the Fe-associated, labile P released to the pore water during this slow crystallization will immediately adsorb to the abundant Fe oxyhydroxides and hence remain captured in the CBD-P pool, while another fraction will precipitate and be ultimately retained as authigenic Ca phosphate minerals (extracted as Ca—P, Fig. 5B, 7B). P:Fe ratios show a minor decrease from the top to the bottom sediment layer at both sites (Fig. 8), implying no significant diffusional loss of P during Fe mineral transformation. The so-called sink-switching of P from Fe-bound to authigenic Ca—P is therefore inhibited due to the persistence of highly reactive Fe phases. Compared to normal deep-sea sediments, where the degradation of organic matter would release significant amounts of P at the sediment-water-interface (Ruttenberg, 2014), we observe hardly any recycling of P in the hydrothermal sediments, as the retention of dissolved PO_4^{3-} is enhanced by the extremely high content and persistence of highly reactive Fe minerals. Furthermore, the sink-switching from Fe-bound P to authigenic Ca—P phases results in the long-term sequestration of substantial amounts of P scavenged from the water column by the hydrothermal precipitates suspended in the buoyant Rainbow plume. Even though the interaction of hydrothermally-sourced Fe and seawater PO_4^{3-} is intense, it remains strongly localized to the close vicinity of the active hydrothermal vents. Overall, it is estimated to account for P removal equivalent to 10–40% of P burial (Feely et al., 1990; Wheat et al., 1996; Wheat et al., 2003). Here, we show that the scavenging of PO_4^{3-} in the Rainbow vent field is very efficient, with very little diagenetic release and recycling observed, in line with previous findings from the east-Pacific Rise (Poulton and Canfield, 2006). As such, hydrothermal sediments are used to reconstruct ancient seawater PO_4^{3-} concentrations (Feely et al., 1998; Bjerrum and Canfield, 2002). An important uncertainty is that variations in seawater chemistry (e.g. dissolved Si concentrations) will strongly affect PO_4^{3-} partitioning between adsorbed and dissolved form and thus the dissolved PO_4^{3-} concentration calculated from solid-phase P/Fe ratio (Konhauser et al., 2007).

5. Conclusions

Our results provide new mechanistic insight into the coupled diagenetic cycles of Fe, P and C in the Rainbow hydrothermal vent field. The suspended particulate matter in the young, buoyant hydrothermal plume seems to of aggregated nanoparticles, comprising both poorly-ordered Fe oxyhydroxides and polycrystalline Fe-sulfides in an organic matrix. The C_{org} in the plume may arise directly from abiotic synthesis in the highly reducing vent fluids and/or be sourced from the chemolithoautotrophic communities that populate the vicinity of the active chimney and the plume. Irrespective of its source, the aggregation and complexation of Fe minerals and organic matter may play a major role in enhancing their dispersion to the deep ocean.

Organic carbon complexation may also represent a controlling factor of preservation of highly-reactive Fe minerals, not only within the plume, but also in the context of long-term burial in the underlying sediments that provide a record of the deposition of mineral-organic

aggregates and suggest a correlation of venting intensity and the burial of C_{org}.

The sorption of PO_4^{3-} by poorly-ordered Fe oxyhydroxides has been shown to only occur in the young, buoyant plume. Scavenging of dissolved seawater PO_4^{3-} is therefore spatially constrained to the early stages of the hydrothermal plume. Phosphorus burial in the hydrothermal sediments is intimately linked to the transport and deposition of Fe oxyhydroxides below the hydrothermal plume. Through sink-switching as well as the abundance and persistence of highly-reactive Fe phases, P is retained efficiently in the sediment, even as the diagenetic transformation of hydrothermal Fe minerals progresses.

Supplementary data to this article can be found online at https://doi.org/10.1016/j.chemgeo.2024.121994.

CRediT authorship contribution statement

Kristin Anna Ungerhofer: Conceptualization, Data curation, Formal analysis, Investigation, Methodology, Visualization, Writing – original draft, Writing – review & editing. **Oliver Plümper:** Formal analysis, Methodology, Supervision, Visualization, Writing – original draft, Writing – review & editing. **Martina Preiner:** Formal analysis, Methodology, Writing – original draft, Writing – review & editing. **Gert-Jan Reichart:** Supervision, Writing – original draft. **Peter Kraal:** Conceptualization, Data curation, Formal analysis, Investigation, Methodology, Visualization, Writing – original draft, Writing – review & editing.

Declaration of competing interest

The authors declare that they have no known competing financial interests or personal relationships that could have appeared to influence the work reported in this paper.

Data availability

Datasets of bulk chemical water-column and sediment chemistry are provided in the Supplementary Information. The full TEM-EDX dataset can be shared upon request to the corresponding author.

Acknowledgments

The Netherlands Initiatives Changing Oceans (NICO) and the NIOZ National Marine Facilities are thanked for ship time and support. We thank the crew and scientific party of Pelagia cruise 64PE441 (chief: Sabine Gollner, NIOZ) for their help with sample collection and processing. In particular, Rick Hennekam is thanked for SPM collection and Karel Bakker for on-board P analyses. Wim Boer of the NIOZ analytical staff is thanked for ICP-MS analyses. We are grateful to Anita van Leeuwen at Utrecht University for XRD analyses. Finally, Lotta Ternieten of Utrecht University is thanked for ATR-IR analysis of two SPM samples.

References

Anderson, L.D., Delaney, M.L., Faul, K.L., 2001. Carbon to phosphorus ratios in sediments: Implications for nutrient cycling. Glob. Biogeochem. Cycles 15 (1), 65–79. https://doi.org/10.1029/2000GB001270.

Anschutz, P., Dedieu, K., Desmazes, F., Chaillou, G., 2005. Speciation, oxidation state, and reactivity of particulate manganese in marine sediments. Chem. Geol. 218 (3–4), 265–279. https://doi.org/10.1016/j.chemgeo.2005.01.008.

APHA, 2005. Standard methods for the examination of water and wastewater. American Public Health Association - American Water Works Association - Water Environment Federation.

Bennett, S.A., Achterberg, E.P., Connelly, D.P., Statham, P.J., Fones, G.R., German, C.R., 2008. The distribution and stabilisation of dissolved Fe in deep-sea hydrothermal plumes. Earth Planet. Sci. Lett. 270 (3–4), 157–167. https://doi.org/10.1016/j.epsl.2008.01.048.

Berner, R.A., 1973. Phosphate removal from seawater by volcanogenic ferric oxides. Earth Planet. Sci. Lett. 18, 77–86.

Bhattarai, B., Pandey, A., Drabold, D.A., 2018. Evolution of amorphous carbon across densities: an inferential study. Carbon. 131, 168–174. https://doi.org/10.1016/j.carbon.2018.01.103.

Bjerrum, C.J., Canfield, D.E., 2002. Ocean productivity before about 1.9 Gyr ago limited by phosphorus adsorption onto iron oxides. Nature 417 (6885), 159–162.

Boström, K., Kraemer, T., Gartner, S., 1973. Provenance and accumulation rates of opaline silica, Al, Ti, Fe, Mn, Cu, Ni and Co in Pacific pelagic sediments. Chem. Geol. 11, 123–148.

Cave, R.R., German, C.R., Thomson, J., Nesbitt, R.W., 2002. Fluxes to sediments underlying the Rainbow hydrothermal plume at 36°14′N on the Mid-Atlantic Ridge. Geochim. Cosmochim. Acta 66 (11), 1905–1923. https://doi.org/10.1016/j.chemgeo.2004.11.015.

Charlou, J.L., Donval, J.P., Fouquet, Y., Jean-Baptiste, P., Holm, N., 2002. Geochemistry of high H2 and CH4 vent fluids issuing from ultramafic rocks at the Rainbow hydrothermal field (36°14′N, MAR). Chem. Geol. 191 (4), 345–359. https://doi.org/10.1016/S0009-2541(02)00134-1.

Claff, S.R., Sullivan, L.A., Burton, E.D., Bush, R.T., 2010. A sequential extraction procedure for acid sulfate soils: Partitioning of iron. Geoderma. 155, 224–230. https://doi.org/10.1016/j.geoderma.2009.12.002.

Cornell, R.M., Schwertmann, U., 2003. The Iron Oxides, second edition. Wiley Verlag GmbH & Co. KGaA, Weinheim.

Douville, E., Charlou, J.L., Oelkers, E.H., Bienvenu, P., Colon, C.F.J., Donval, J.P., Fouquet, Y., Prieur, D., Appriou, P., 2002. The rainbow vent fluids (36°14VN, MAR): the influence of ultramafic rocks and phase separation on trace metal content in Mid-Atlantic Ridge hydrothermal fluids. Chem. Geol. 184, 37–48.

Dyment, J., 2009. Detailed Investigation of Hydrothermal Site Rainbow, Mid-Atlantic Ridge, 36°13'N: Cruise MoMARDream. IFREMER.

Edmonds, H.N., German, C.R., 2004. Particle geochemistry in the Rainbow hydrothermal plume, Mid-Atlantic Ridge. Geochim. Cosmochim. Acta 68 (4), 759–772. https://doi.org/10.1016/S0016-7037(03)00498-8.

Fagerbakke, K.M., Heldal, M., Norland, S., 1996. Content of carbon, nitrogen, oxygen, sulfur and phosphorus in native aquatic and cultured bacteria. Aquat. Microb. Ecol. 10 (1), 15–27. https://doi.org/10.3354/ame010015.

Faust, J.C., Tessin, A., Fisher, B.J., Zindorf, M., Papadaki, S., Hendry, K.R., Doyle, K.A., März, C., 2021. Millennial scale persistence of organic carbon bound to iron in Arctic marine sediments. Nat. Commun. https://doi.org/10.1038/s41467-020-20550-0.

Feely, R.A., Massoth, G.J., Baker, E.T., Cowen, J.P., Lamb, M.F., Krogslund, K.A., 1990. The effect of hydrothermal processes on midwater phosphorus distributions in the Northeast Pacific. Earth Planet. Sci. Lett. 96, 305–318.

Feely, R.A., Trefry, J.H., Massoth, G.J., Metz, S., 1991. A comparison of the scavenging of phosphorus and arsenic from seawater by hydrothermal iron oxyhydroxides in the Atlantic and Pacific Oceans. Deep Sea Res. Part A, Oceanograph. Res. Paper. 38 (6), 617–623. https://doi.org/10.1016/0198-0149(91)90001-V.

Feely, R.A., Trefry, J.H., Lebon, G.T., German, C.R., 1998. The relationship between P/Fe and V/Fe ratios in hydrothermal precipitates and dissolved phosphate in seawater. Geophys. Res. Lett. 25 (13), 2253–2256. https://doi.org/10.1029/98GL01546.

Findlay, A.J., Estes, E.R., Gartman, A., Yücel, M., Kamyshny, A., Luther, G.W., 2019. Iron and sulfide nanoparticle formation and transport in nascent hydrothermal vent plumes. Nat. Commun. 10 (1), 1–7. https://doi.org/10.1038/s41467-019-09580-5.

Fitzsimmons, J.N., John, S.G., Marsay, C.M., Hoffman, C.L., Nicholas, S.L., Toner, B.M., German, C.R., Sherrell, R.M., 2017. Iron persistence in a distal hydrothermal plume supported by dissolved-particulate exchange. Nat. Geosci. 10 (3), 195–201. https://doi.org/10.1038/ngeo2900.

Fröhlich, P.N., Bender, M.L., Luedtke, N.A., 1982. The marine phosphorus cycle. Am. J. Sci. 282, 474–511.

Gartman, A., Findlay, A.J., Luther, G.W., 2014. Nanoparticulate pyrite and other nanoparticles are a widespread component of hydrothermal vent black smoker emissions. Chem. Geol. 366, 32–41. https://doi.org/10.1016/j.chemgeo.2013.12.013.

German, C.R., Seyfried, W.E., 2014. Hydrothermal Processes. In: Treatise on Geochemistry, , Second ed.8. Elsevier Ltd. https://doi.org/10.1016/B978-0-08-095975-7.00607-0

German, C.R., Klinkhammer, G.P., Rudnicki, M.D., 1996. The Rainbow hydrothermal plume, 36°15′N, MAR, 23 (21), 2979–2982.

German, C., Richards, K., Lam, M., Charlou, J., Scientific Party, F., 1998. Topographic control of a dispersing hydrothermal plume. Earth Planet. Sci. Lett. 156, 267–273.

German, C.R., Legendre, L.L., Sander, S.G., Niquil, N., Luther, G.W., Bharati, L., Han, X., Le Bris, N., 2015. Hydrothermal Fe cycling and deep ocean organic carbon scavenging: Model-based evidence for significant POC supply to seafloor sediments. Earth Planet. Sci. Lett. 419, 143–153. https://doi.org/10.1016/j.epsl.2015.03.012.

González-Santana, D., González-Dávila, M., Lohan, M.C., Artigue, L., Ne Planquette, H., Sarthou, G., Tagliabue, A., Santana-Casiano, J.M., 2021. Variability in iron (II) oxidation kinetics across diverse hydrothermal sites on the northern Mid Atlantic Ridge. Geochem. et Chosmochim. Acta 297, 143–157. https://doi.org/10.1016/j.gca.2021.01.013.

Grasshoff, K., Kremling, K., Ehrhardt, M., 1983. Methods of Seawater Analysis. WILEY-VCH Verlag GmbH.

Haalboom, S., Price, D.M., Mienis, F., van Bleijswijk, J.D.L., de Stigter, H.C., Witte, H.J., Reichart, G.-J., Duineveld, G.C.A., 2020. Patterns of (trace) metals and microorganisms in the Rainbow hydrothermal vent plume at the Mid-Atlantic Ridge. Biogeosciences. 17 (9), 2499–2519. https://doi.org/10.5194/bg-17-2499-2020.

Hawkes, J.A., Connelly, D.P., Gledhill, M., Achterberg, E.P., 2013. The stabilisation and transportation of dissolved iron from high temperature hydrothermal vent systems. Earth Planet. Sci. Lett. 375, 280–290. https://doi.org/10.1016/j.epsl.2013.05.047.

Hayes, C.T., Costa, K.M., Anderson, R.F., Calvo, E., Chase, Z., Demina, L.L., Dutay, J.-C., German, C.R., Heimbürger-Boavida, L.-E., Jaccard, S.L., Jacobel, A., Kohfeld, K.E.,

Kravchishina, M.D., Lippold, J., Mekik, F., Missiaen, L., Pavia, F.J., Paytan, A., Pedrosa-Pamies, R., Petrova, M.V., Rahman, S., Robinson, L.F., Roy-Barman, M., Sanchez-Vidal, A., Shiller, A., Tagliabue, A., Tessin, A.C., van Hulten, M., Zhang, J., 2021. Global Ocean Sediment Composition and Burial Flux in the Deep Sea. Global Biogeochem. Cycles 35 (4), e2020GB006769.

Helder, W., De Vries, R.T.P., 1979. An automatic phenol-hypochlorite method for the determination of ammonia in sea- and brackish waters. Neth. J. Sea Res. 13 (1), 154–160.

Hemingway, J.D., Rothman, D.H., Grant, K.E., Rosengard, S.Z., Eglinton, T.I., Derry, L.A., Galy, V.V., 2019. Mineral protection regulates long-term global preservation of natural organic carbon. Nature. 570 (7760) https://doi.org/10.1038/s41586-019-1280-6.

Holm, N.G., Charlou, J.L., 2001. Initial indications of abiotic formation of hydrocarbons in the Rainbow ultramafic hydrothermal system, Mid-Atlantic Ridge. Earth Planet. Sci. Lett. 191 (1), 1–8. https://doi.org/10.1016/S0012-821X(01)00397-1.

Khripounoff, A., Vangriesheim, A., Crassous, P., Crassous, P., Segonzac, M., Colaço, A., Desbruyères, D., Barthelemy, R., 2001. Particle flux in the Rainbow hydrothermal vent field (Mid-Atlantic Ridge): Dynamics, mineral and biological composition. J. Mar. Res. 59 (4), 633–656. https://doi.org/10.1357/002224001762842217.

Konhauser, K.O., Lalonde, S.V., Amskold, L., Holland, H.D., 2007. Was there really an Archean Phosphate Crisis? Science 315 (5816), 1234. https://doi.org/10.1126/science.1136328.

Konn, C., Charlou, J.L., Donval, J.P., Holm, N.G., Dehairs, F., Bouillon, S., 2009. Hydrocarbons and oxidized organic compounds in hydrothermal fluids from Rainbow and lost City ultramafic-hosted vents. Chem. Geol. 258 (3), 299–314. https://doi.org/10.1016/j.chemgeo.2008.10.034.

Kraal, P., Dijkstra, N., Behrends, T., Slomp, C.P., 2017. Phosphorus burial in sediments of the sulfidic deep Black Sea: Key roles for adsorption by calcium carbonate and apatite authigenesis. Geochim. Cosmochim. Acta 204, 140–158. https://doi.org/10.1016/j.gca.2017.01.042.

Kraal, P., van Genuchten, C.M., Behrends, T., Rose, A.L., 2019. Sorption of phosphate and silicate alters dissolution kinetics of poorly crystalline iron (oxyhydr)oxide. Chemosphere. 234, 690–701. https://doi.org/10.1016/j.chemosphere.2019.06.071.

Kraal, P., van Genuchten, C.M., Behrends, T., 2022. Phosphate coprecipitation affects reactivity of iron (oxyhydr)oxides towards dissolved iron and sulfide. Geochim. Cosmochim. Acta 321, 311–328. https://doi.org/10.1016/j.gca.2021.12.032.

Krom, M.D., Berner, R.A., 1980. Adsorption of phosphate in anoxic marine sediments. Limnol. Oceanogr. 25 (5), 797–806. https://doi.org/10.4319/lo.1980.25.5.0797.

Lalonde, K., Mucci, A., Ouellet, A., Gélinas, Y., 2012. Preservation of organic matter in sediments promoted by iron. Nature. 483 (7388), 198–200. https://doi.org/10.1038/nature10855.

Li, M., Toner, B.M., Baker, B.J., Breier, J.A., Sheik, C.S., Dick, G.J., 2014. Microbial iron uptake as a mechanism for dispersing iron from deep-sea hydrothermal vents. Nat. Commun. 5 (1), 1–8. https://doi.org/10.1038/ncomms4192.

McCollom, T.M., 2000. Geochemical constraints on primary productivity in submarine hydrothermal vent plumes. Deep-Sea Res. I Oceanogr. Res. Pap. 47 (1), 85–101. https://doi.org/10.1016/S0967-0637(99)00048-5.

McIver, R.D., 1975, May 11. PD 5(l) hydrocarbon occurrences from joides deep sea drilling project. In: 9th World Petroleum Congress. In: https://onepetro.org/WPCONGRESS/proceedings-abstract/WPC09/All-WPC09/199273.

Murphy, J., Riley, J.P., 1958. A single-solution method for the determination of soluble phosphate in sea water. J. Mar. Biol. Assoc. U. K. 37 (1), 9–14. https://doi.org/10.1017/S0025315400014776.

Needoba, J.A., Foster, R.A., Sakamoto, C., Zehr, J.P., Johnson, K.S., 2007. Nitrogen fixation by unicellular diazotrophic cyanobacteria in the temperate oligotrophic North Pacific Ocean. Limnol. Oceanogr. 52 (4), 1317–1327. https://doi.org/10.4319/lo.2007.52.4.1317.

Poulton, S.W., Canfield, D.E., 2005. Development of a sequential extraction procedure for iron: Implications for iron partitioning in continentally derived particulates. Chem. Geol. 214, 209–221. https://doi.org/10.1016/j.chemgeo.2004.09.003.

Poulton, S.W., Canfield, D.E., 2006. Co-diagenesis of iron and phosphorus in hydrothermal sediments from the southern East Pacific rise: Implications for the evaluation of paleoseawater phosphate concentrations. Geochim. Cosmochim. Acta 70, 5883–5898. https://doi.org/10.1016/j.gca.2006.01.030.

Redfield, A.C., 1958. The biological control of chemical factors in the environment. Am. Sci. 46 (3), 205–221.

Roohi, R., Hoogenboom, R., Van Bommel, R., Van Der Meer, M.T.J., Mienis, F., Gollner, S., 2022. Influence of Chemoautotrophic Organic Carbon on Sediment and its Infauna in the Vicinity of the Rainbow Vent Field. Front. Mar. Sci. 9 https://doi.org/10.3389/FMARS.2022.732740/FULL.

Ruttenberg, C., 1992. Development of a sequential extraction method for different forms of phosphorus in marine sediments. Limnol. Oceanogr. 37 (7), 1460–1482.

Ruttenberg, K.C., 2014. The phosphorus cycle. Aquat. Ecol. 6, 347–363. https://doi.org/10.1007/978-94-017-8944-8_20.

Sander, S.G., Koschinsky, A., 2011. Metal flux from hydrothermal vents increased by organic complexation. Nat. Geosci. 4 (3) https://doi.org/10.1038/ngeo1088. Article 3.

Shock, E.L., Schulte, M.D., 1998. Organic synthesis during fluid mixing in hydrothermal systems. J. Geophys. Res.: Planet. 103 (E12), 28513–28527.

Slomp, C.P., Epping, E.H.G., Helder, W., Van Raaphorst, W., 1996. A key role for iron-bound phosphorus in authigenic apatite formation in North Atlantic continental platform sediments. J. Mar. Res. 54 (6), 1179–1205. https://doi.org/10.1357/0022240963213745.

Tagliabue, A., Bopp, L., Dutay, J.-C., Bowie, A.R., Chever, F., Jean-Baptiste, P., Bucciarelli, E., Lannuzel, D., Remenyi, T., Sarthou, G., Aumont, O., Gehlen, M., Jeandel, C., 2010. Hydrothermal contribution to the oceanic dissolved iron inventory. Nat. Geosci. 3 (4), 252–256. https://doi.org/10.1038/ngeo818.

Tebo, B.M., Bargar, J.R., Clement, B.G., Dick, G.J., Murray, K.J., Parker, D., Verity, R., Webb, S.M., 2004. Biogenic Manganese Oxides: Properties and Mechanisms of Formation. Annu. Rev. Earth Planet. Sci. 32 (1), 287–328. https://doi.org/10.1146/annurev.earth.32.101802.120213.

Thurnherr, A.M., Richards, K.J., 2001. Hydrography and high-temperature heat flux of the Rainbow hydrothermal site (36°14′N, Mid-Atlantic Ridge). J. Geophys. Res. Oceans 106 (C5), 9411–9426. https://doi.org/10.1029/2000jc900164.

Toner, B.M., Fakra, S.C., Manganini, S.J., Santelli, C.M., Marcus, M.A., Moffett, J.W., Rouxel, O., German, C.R., Edwards, K.J., 2009. Preservation of iron(II) by carbon-rich matrices in a hydrothermal plume. Nat. Geosci. 2 (3), 197–201. https://doi.org/10.1038/ngeo433.

Trocine, R.P., Trefry, J.H., 1988. Distribution and chemistry of suspended particles from an active hydrothermal vent site on the Mid-Atlantic Ridge at 26°N. Earth Planet. Sci. Lett. 88 (1), 1–15. https://doi.org/10.1016/0012-821X(88)90041-6.

Turekian, K.K., Wedepohl, K.H., 1961. Distribution of the elements in some major units of the Earth's crust. Geol. Soc. Am. Bull. 72 (2), 175–192.

Van der Zee, C., Roberts, D.R., Rancourt, D.G., Slomp, C.P., 2003. Nanogoethite is the dominant reactive oxyhydroxide phase in lake and marine sediments. Geology. 31 (11), 993–996. https://doi.org/10.1130/G19924.1.

Van Loon, D., 2016. Effect of Hydrothermal Vent Activity of the Rainbow Vent Field (Mid Atlantic Ridge) on Sediment Geochemistry. MSc thesis.. Netherlands Institute for Sea Research.

Verardo, D.J., Froehlich, P.N., McIntyre, A., 1990. Determination of organic carbon and nitrogen in marine sediments using the Carlo Erba NA-1500 Analyzer. Deep-Sea Res. 37 (1), 157–165. https://doi.org/10.3189/s0022143000024291.

Voegelin, A., Senn, A.-C., Kaegi, R., Hug, S.J., Mangold, S., 2013. Dynamic Fe-precipitate formation induced by Fe(II) oxidation in aerated phosphate-containing water. Geochim. Cosmochim. Acta 117, 216–231. https://doi.org/10.1016/j.gca.2013.04.022.

Vrede, K., Heldal, M., Norland, S., Bratbak, G., 2002. Elemental composition (C, N, P) and cell volume of exponentially growing and nutrient-limited bacterioplankton. Appl. Environ. Microbiol. 68 (6), 2965–2971.

Wheat, C.G., Feely, R.A., Mom, M.J., 1996. Phosphate removal by oceanic hydrothermal processes: an update of the phosphorus budget in the oceans. Geochim. Cosmochim. Acta 60 (19), 3593–3608.

Wheat, C.G., McManus, J., Mottl, M.J., Giambalvo, E., 2003. Oceanic phosphorus imbalance: Magnitude of the mid-ocean ridge flank hydrothermal sink. Geophys. Res. Lett. 30 (17) https://doi.org/10.1029/2003GL017318.

Yücel, M., Gartman, A., Chan, C.S., Luther, G.W., 2011. Hydrothermal vents as a kinetically stable source of iron-sulphide-bearing nanoparticles to the ocean. Nat. Geosci. 4 (6), 367–371. https://doi.org/10.1038/ngeo1148.

Zhao, J., Huggins, F.E., Feng, Z., Huffman, G.P., 1994. Ferrihydrite: Surface Structure and Its Effects on Phase Transformation. Clays and Clay Minerals 42 (6), 737–746.